AGU ADVANCING EARTH AND SPACE SCIENCE

JGR Atmospheres

RESEARCH ARTICLE
10.1029/2021JD036157

Key Points:

- Benefits of using additive inflation and adaptive observation error during infrared radiance assimilation are demonstrated
- The adaptive observation error improves the relative weights given to radiance and reflectivity observations during assimilation
- A benefit of assimilating Advanced Baseline Imager channel 9 radiance, in addition to channel 10, is demonstrated for this case study

Correspondence to:
A. Johnson,
ajohns14@ou.edu

Citation:
Johnson, A., Wang, X., & Jones, T. (2022). Impacts of assimilating GOES-16 ABI channels 9 and 10 clear air and cloudy radiance observations with additive inflation and adaptive observation error in GSI-EnKF for a case of rapidly evolving severe supercells. *Journal of Geophysical Research: Atmospheres*, *127*, e2021JD036157. https://doi.org/10.1029/2021JD036157

Received 4 NOV 2021
Accepted 11 MAY 2022

Impacts of Assimilating GOES-16 ABI Channels 9 and 10 Clear Air and Cloudy Radiance Observations With Additive Inflation and Adaptive Observation Error in GSI-EnKF for a Case of Rapidly Evolving Severe Supercells

Aaron Johnson[1], Xuguang Wang[1], and Thomas Jones[2,3]

[1]School of Meteorology, University of Oklahoma, Norman, OK, USA, [2]Cooperative Institute for Mesoscale Meteorological Studies, University of Oklahoma, Norman, OK, USA, [3]National Severe Storms Laboratory, University of Oklahoma, Norman, OK, USA

Abstract The unprecedentedly high space and time resolution of infrared radiance observations from GOES-16 Advanced Baseline Imager (ABI) present an opportunity to improve analyses and short-term forecasts of rapidly evolving convective-scale processes such as the initiation and organization of severe supercell thunderstorms. Such a case is used for experiments aimed at better understanding the assimilation of ABI all-sky radiance observations in GSI-EnKF. Experiments assimilating ABI channel 10 are used to demonstrate and understand the impacts of implementing additive inflation and adaptive observation error for ABI radiance assimilation in GSI-EnKF. The experiments using channel 10 are then compared to experiments using ABI channel 9 and both channels together. The impact of additive inflation is to increase lead time of one of the two supercells by about 20 min, and to enable improved prediction of the second supercell. The improvement occurs because the development of deepening cumulus is accelerated where ABI observes clouds to appear that are not present in the ensemble background forecast. The impact of the adaptive observation error is to increase the strength and persistence of the developing supercells in forecasts initialized from ensemble mean analyses. Compared to the ABI channel 10 radiance, ABI channel 9 provides 10 min of additional lead time for the second supercell, likely because it better constrains an upper-level shortwave in clear air.

Plain Language Summary The GOES-16 satellite is capable of infrared radiance observations at higher time and space resolutions than previously available. The assimilation of such observations into forecast models has the potential to improve short-term forecasts of convective systems that evolve on time and space scales comparable to the radiance observations. Since radar reflectivity observations also provide information on similar space and time scales, research is needed on methods to harmoniously assimilate both data sets in a way that takes advantage of the strengths of both the satellite-based radiance and ground-based reflectivity. This study explores two such methods, additive inflation and adaptive observation error, to better understand the impacts of these techniques on the resulting analysis and subsequent forecast obtained from assimilating radiance and reflectivity observations together. Furthermore, experiments assimilating different infrared channels that observe upper-level and mid-level features are conducted. These experiments use a case study of rapidly developing supercell thunderstorms which provide unique challenges that the convective scale assimilation is uniquely suited to address. We conclude that both additive inflation and adaptive observation error improve the simultaneous assimilation of reflectivity and radiance observations, while channel 9 and channel 10 do provide unique information resulting in improved forecast when both channels are included.

1. Introduction

The Advanced Baseline Imager (ABI) instrument on the geostationary National Oceanographic and Atmospheric Administration (NOAA) GOES-16 satellite provides continuous coverage over the United States with unprecedentedly high spatial (about 2 km) and temporal (about every 5 min) coverage. The ABI infrared (IR) observations are expected to be particularly well suited to address the challenges of predicting the early stages of convection initiation (CI) and the rapid evolution of convective-scale systems (Schröttle et al., 2021). Such systems typically evolve on time scales of minutes and space scales of kilometers. These space and time scales are consistent with the ABI resolution and are much finer than existing in situ observation networks.

Radar observations have resolutions comparable to that of the ABI and provide information about the convective scale structure of well-developed precipitating convection. However, radar reflectivity is typically not well suited to detecting non-precipitating cloud features which sometimes indicates the early stages of CI. Ground-based radar also provides incomplete observations of convective-scale processes above the storm at the tropopause level. The upper levels of convective systems can play important roles in blocking insolation from surrounding areas (Overthaler & Markowski, 2013) and indicating the strength of storm updrafts (Bedka & Khlopenkov, 2016). Satellite-based all-sky IR radiance is well suited to observe the upper levels of mature convection, as well as detecting the CI process before substantial precipitating hydrometeors are detected by radar (R. D. Roberts & Rutledge, 2003). IR radiance can also provide information about the pre-convective and near-convective mid-tropospheric environment in clear air such as destabilization or moistening corresponding to mesoscale ascent (e.g., Koenig & de Coning, 2009). However, the impacts on convective scale forecast performance of different techniques for assimilating ABI radiances are not yet fully understood. As a first step toward better understanding the systematic impacts on forecast performance of such techniques, there is a need to document the physical impacts of each technique in isolation.

Several studies have shown the benefits of assimilating ABI all-sky IR radiances in the low-level water vapor channel (i.e., channel 10, or 7.3 micron) for short-term forecasts of organized convective storms, including both supercells and mesoscale convective systems (e.g., Jones et al., 2020; Y. Zhang et al., 2019, 2018). Y. Zhang et al. (2018) assimilated all-sky radiances from ABI channel 10 with adaptive observation error inflation (AOEI) and adaptive background error inflation (ABEI) and found that they improved supercell forecasts both by reducing spurious cloud in the analysis and by improving analyses of (mainly ice phase) hydrometeors. The ABEI functioned by inflating background ensemble spread when the mismatch between observed radiance and ensemble mean background radiance (i.e., innovation) is large. However, in some cases all ensemble members may fail to initiate deep convection near an observed storm, resulting in near-zero background spread of the hydrometeor and other variables related to deep convection. In such cases, alternative methods of correcting the ensemble background spread may be beneficial for the ABI assimilation. Therefore, an alternative approach is introduced in the present study following an additive inflation approach often used in radar reflectivity data assimilation. Additive inflation is often used in radar DA, especially during the early stages of convection where the model background ensemble can miss the storms resulting in poor background error covariance on the convective scale (Dowell & Wicker, 2009; Sobash & Wicker, 2015). The impacts of similar additive inflation applied to all-sky radiance assimilation have not yet been studied. The present study extends the additive inflation method to ABI all-sky radiance assimilation with the goal of physical understanding of its impact on a case of rapidly developing supercells.

Other studies have also demonstrated advantages of assimilating both clear-sky and all-sky radiances, although without focusing specifically on short-term forecasts of organized convection (Cintineo et al., 2016; Jones et al., 2013, 2014; Ma et al., 2017; Otkin & Potthast, 2019). The harmonious assimilation of such diverse remotely sensed data that constrain different aspects of the analysis is also an important consideration (Pan et al., 2018). Ideally, the different sources of observations would complement, without limiting the advantages, of the other observations. The AOEI in Y. Zhang et al. (2018) functioned by inflating observation error when the innovation is large to account for representativeness errors inferred from the fact that a radiance observation outside of the ensemble envelope can be associated with model state variables still within the ensemble envelope (Minamide & Zhang, 2017). In OSSE experiments with a tropical cyclone case, the AOEI was preferred over an alternative method that inflates observation error based on a symmetric cloud effect that quantifies discrepancies between simulated and observed cloud cover (Minamide & Zhang, 2017). The AOEI was preferred because it only inflated observation error in smaller-scale regions with large innovation, allowing the ABI radiance to have greater impact on the analysis increment in regions with smaller innovations but large symmetric cloud affect. However, in cases of continental convection with broad convective anvil clouds and simultaneous availability of radar reflectivity observations, the impact of observation errors on the relative weight given to different observation types during data assimilation should also be considered. In particular, we hypothesize that the observation error inflation based on symmetric cloud effect can facilitate harmonious assimilation of the ABI radiance and radar reflectivity observations by affecting the relative impact of radiance and reflectivity observations on the analysis. The estimation of radiance observation errors as a function of the cloud impact (Geer & Bauer, 2011; Harnisch et al., 2016; Okamoto et al., 2014) has also not been fully explored in the specific context of the newly available ABI all-sky radiance assimilation or for rapidly developing storms. The present study applies an adaptive observation error based on symmetric cloud effect to a real-data (non-OSSE) case of rapidly developing supercells with the goal of physically understanding its impact on analysis and forecast quality.

Early studies of all-sky ABI radiance assimilation only ingested a single water vapor channel (e.g., Minamide & Zhang, 2017; Y. Zhang et al., 2018). While multiple channels have been assimilated in clear air (Hutt et al., 2020), the effect of assimilating multiple channels has not yet been investigated in the context of all-sky assimilation for convective-scale forecasts. This is in part due to a desire to avoid potential complications resulting from correlations among observation errors in different channels (Geer, 2019; Honda et al., 2018). Multiple channels were assimilated in Xu et al. (2021) but the impact of assimilating multiple channels was not evaluated. The assimilation of multiple channels in clear air has the advantage of obtaining information about the vertical structure of the atmosphere because the radiance weighting functions peak at different levels. Assimilating multiple channels may also be advantageous in some cloudy pixels where the channel difference can provide information about cloud depth. However, it is also conceivable that assimilating multiple channels in this context could degrade analysis and forecast quality because correlations of observation errors from the different channels violate the assumptions of the ensemble Kalman filter, especially in cloudy pixels. Therefore, a third goal of the present study is to investigate the physical impacts of assimilating two different IR water vapor channels in the context of rapidly developing supercells. ABI channels 9 (weighting function maximum at ∼400 hPa) and 10 (weighting function maximum at ∼625 hPa) are selected for this experiment. Channel 10 is selected because it has been commonly used in similar applications (e.g., Y. Zhang et al., 2018). Channel 9 is selected, rather than channel 8, because there exists substantial overlap in the channel 9 and channel 10 weighting functions which may result in correlated observation errors, even in clear air. Therefore, it is less clear a priori whether a forecast can be improved by assimilating a second ABI channel when adding channel 9 than when adding channel 8.

In summary, the present study uses a case study of rapidly developing supercells to demonstrate physical impacts of three specific techniques for the assimilation of all-sky ABI radiance water vapor channels in a convective-scale model. In particular, the techniques of additive inflation, adaptive observation error, and two-channel assimilation are applied and evaluated. While systematic evaluation over many forecasts will also be needed to determine optimal configurations, the scope of the present study is limited to achieving physical understanding of the impacts of the additive inflation, adaptive observation error, and two-channel assimilation in this case study through detailed diagnostics. The remainder of this paper is organized as follows. Section 2 contains an overview of the case study and the details of the methods and experiment design. Results are presented in Section 3 while Section 4 includes a summary and conclusions.

2. Methods

2.1. Case Study Overview

A case study from 18 May 2017 of two long-track supercells that initiated and rapidly matured is adopted in order to focus on a case when the ABI data are expected to be particularly beneficial in the context of a frequently cycled DA and short-term forecast system. This case is also selected because of spurious cloud cover and a lack of deep convection in the region of interest in the model first guess forecasts which create unique challenges for both reflectivity and radiance assimilation for this case, as discussed further in Section 3.1. The case is characterized by a large-scale upper-level trough over the western U.S. associated with 30–40 m s^{-1} of west-southwesterly diffluent flow at 250 hPa over southwest Oklahoma and northwest Texas (Figure 1a). At low levels, high pressure over the southeast U.S. induced southerly flow of warm, moist air with an origin over the Gulf of Mexico. A dryline, indicated by an abrupt wind shift and moisture gradient, was located in west Texas (Figures 1b and 1c).

Multiple vorticity maxima embedded in the southwesterly flow at upper levels were present in the National Centers for Environmental Prediction (NCEP) Global Forecast System (GFS) analysis at 18:00 UTC (Figures 1d–1f). In particular, there were mesoscale vorticity maxima from northwest Texas into southeast New Mexico at 300 hPa (Figure 1d; circled region) and from west into southwest Texas at 400 hPa (Figure 1f; circled region). The increasing cyclonic vorticity advection with height in advance of these features would be expected to induce rising motion which may have contributed to weakening convective inhibition before CI (e.g., S.-Y. Wang et al., 2009). These features are particularly interesting for this study due to their location on the west side of trough axes in the moisture field (red contours and thick green arc in Figures 1d and 1f). Given the co-location of these features in the GFS analysis, and the potential for dynamical links between upper-level dry intrusions and vorticity maxima

10.1029/2021JD036157

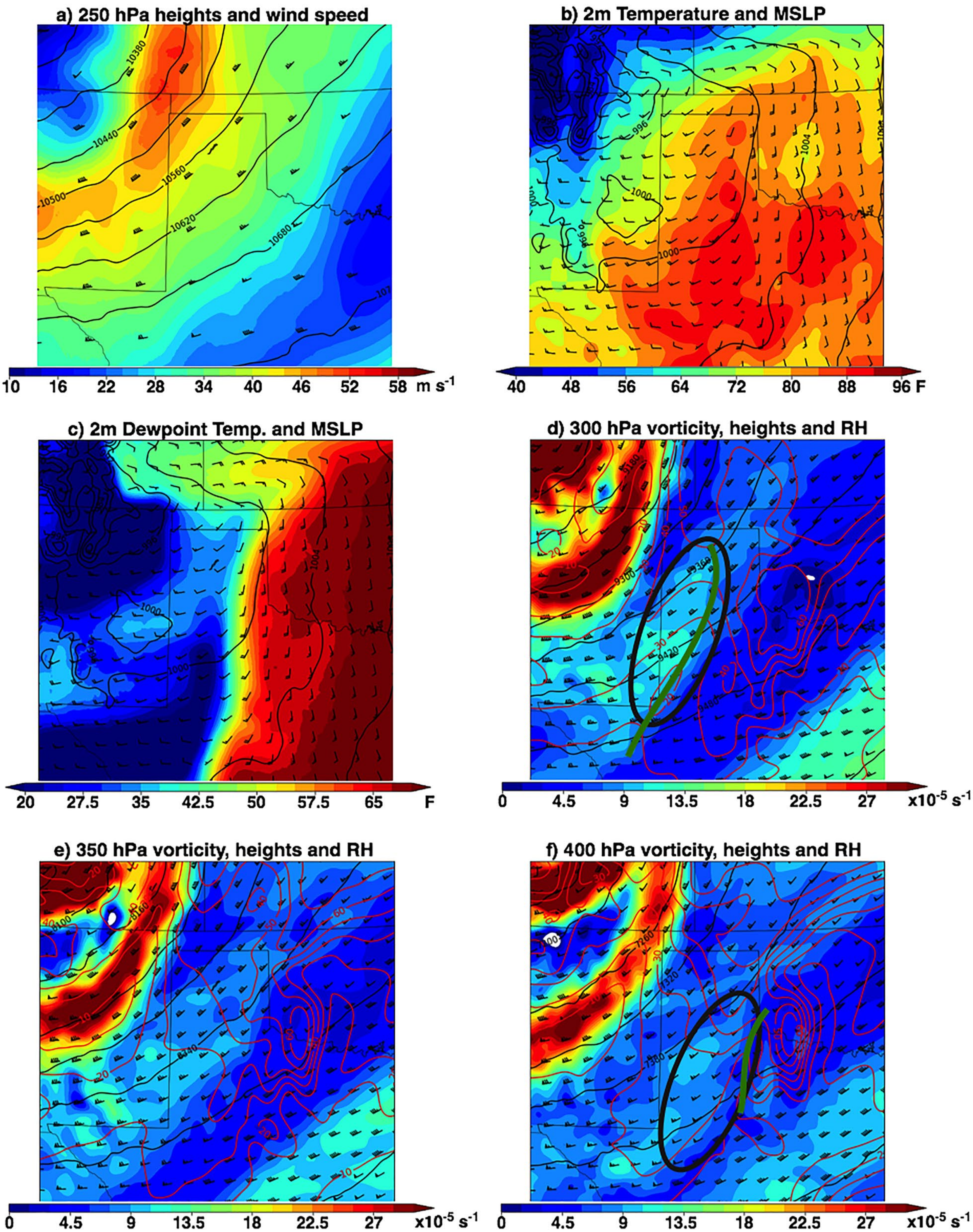

Figure 1.

10.1029/2021JD036157

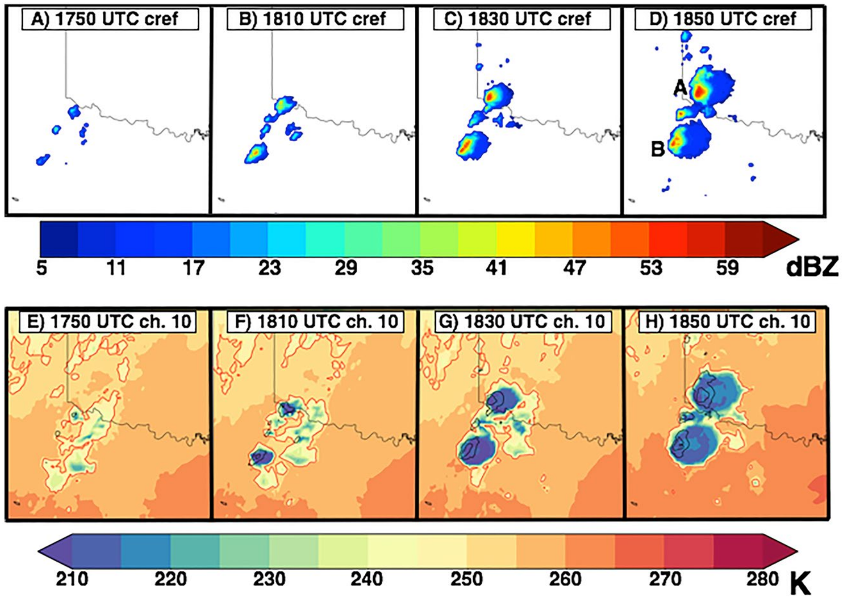

Figure 2. Panels (a–d) show MRMS composite reflectivity at (a) 17:50 UTC, (b) 18:10 UTC, (c) 18:30 UTC, and (d) 18:50 UTC. Labels "A" and "B" on panel (d) indicate the storms referred to in the text as the "northernmost" and "southernmost" supercell, respectively. Panels (e–h) show ABI channel 10 brightness temperature (shading), MRMS composite reflectivity (black contours every 20 dBZ) and cloud-affected brightness temperature determined using BT_{lim} (red contour) at (e) 17:50 UTC, (f) 18:10 UTC, (g) 18:30 UTC, and (h) 18:50 UTC.

(Muller & Fuelberg, 1990), the ABI radiances are expected to improve analyses of vorticity maxima contributing to the CI event as well as the early stages of convective scale cumulus deepening.

Composite reflectivity from NEXRAD, in the quality-controlled Multi-Radar Multi-Sensor (MRMS; J. Zhang et al., 2016) data set, detected the CI starting between 17:50 and 18:10 UTC on 18 May (Figures 2a and 2b). A low-level cumulus field developed in visible satellite imagery at least an hour before the radar-detected CI, and brightness temperatures (BTs) below 220 K indicating development of towering cumulus was detected in IR satellite imagery tens of minutes before the radar-detected CI (Figure 2e). The two storms that initiated around 18:00 UTC quickly strengthened into two dominant discrete supercells. These storms are referred to in this paper as the "northernmost" storm and "southernmost" storm and are labeled in Figure 2d as storms "A" and "B", respectively. These supercells were associated with long paths of severe weather reports, primarily large hail and one tornado (not shown).

2.2. Forecast Model Configuration

This study uses the Weather Research and Forecasting (WRF) Advanced Research WRF (ARW) model version 3.9.1 (Skamarock et al., 2008) with 3 km grid spacing over the domain covering the continental United States shown in Gasperoni et al. (2020; their Figure 1). The physics configuration includes Thompson et al. (2008) microphysics, Mellor-Yamada-Nakanishi-Niino (MYNN; Nakanishi & Niino, 2009) planetary boundary layer, RUC land surface model (Benjamin et al., 2004), and rapid radiative transfer model (RRTMG; Mlawer et al., 1997) short-wave and long-wave radiation parameterizations. The model is configured with 50 vertical levels with 50 hPa model top, following Gasperoni et al. (2020).

Figure 1. NCEP GFS 18:00 UTC 18 May 2017 analysis of (a) 250 hPa geopotential height (black contours; m) wind speed (shading; m s^{-1}) and wind barbs, (b) 2 m temperature (shading), MSLP (black contours; hPa) and 10 m wind barbs, (c) 2 m dewpoint temperature (shading), MSLP (black contours; hPa) and 10 m wind barbs, (d) 300 hPa geopotential height (black contours; m), vorticity (shading; x10^{-5} s^{-1}), wind barbs and relative humidity (red contours; %), (e) as in (d) except at 350 hPa, and (f) as in (d) except at 400 hPa. Black ellipse on panels (d and f) highlight vorticity maxima discussed in the text. Thick green arcs on panels (d and f) highlight relative humidity troughs discussed in the text.

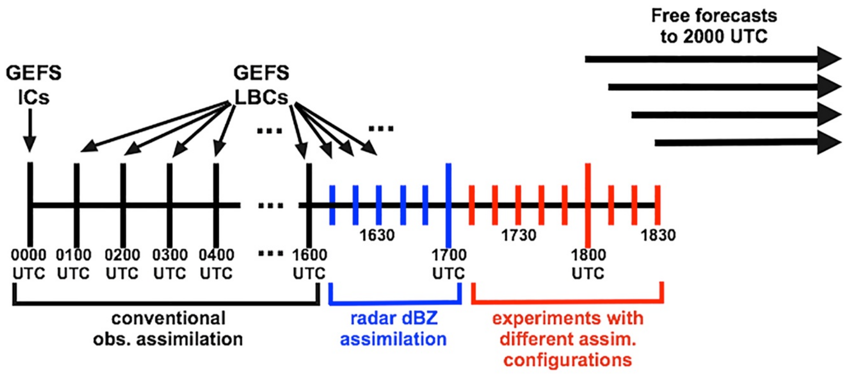

Figure 3. Diagram of DA and forecast system configuration.

2.3. DA System Configuration

The DA system is the GSI-EnKF (X. Wang & Lei, 2014; X. Wang et al., 2013; Whitaker et al., 2008) that was already extended to include the direct assimilation of reflectivity from ground-based radars (Johnson et al., 2015; Y. Wang & Wang, 2017), and is herein modified to include direct assimilation of all-sky radiances from ABI. The Community Radiative Transfer Model (CRTM) version 2.3 (Han et al., 2006) is used within GSI to provide model priors of observed radiance, considering all cloud and hydrometeor species in the Thompson et al. (2008) microphysics scheme adopted for this study. This study builds on the GSI-EnKF system that was previously extended in Y. Wang and Wang (2017) to now ingest the ABI observations, recognize "abi" as an observation type, extend the state vector to include snow, ice, and graupel hydrometeors, and link to the CRTM static coefficients for ABI radiance.

A 40-member fixed-physics ensemble is used for the EnKF, with initial and lateral boundary conditions from the 00:00 UTC 18 May and 18:00 UTC 17 May cycles of the NCEP Global Ensemble Forecast System (GEFS; Zhou et al., 2017) for the first and second 20 ensemble members, respectively. The 0 hr (first 20 members) and 6 hr (second 20 members) GEFS forecasts are used to maintain spread while initializing a larger ensemble than the GEFS ensemble. Hourly assimilation of conventional surface and upper-air observations is conducted from 01:00 to 16:00 UTC on 18 May (Figure 3). The purpose of the conventional observation assimilation is to spin up ensemble mean and spread of the synoptic to mesoscale environment consistent with the WRF model climate and resolution using the observations, while minimizing the impact of any deficiencies in the coarse resolution initial ensemble from 00:00 UTC 18 May. Radar reflectivity data from MRMS mosaics with 1 km vertical resolution (J. Zhang et al., 2016) are then assimilated every 10 min from 16:10 to 17:00 UTC to help suppress some spurious cloud and precipitation that possibly resulted from errors originating with the GEFS initial conditions on this case. The spurious cloud was not fully suppressed by the conventional observations alone. ABI is not assimilated during 16:10–17:00 in order to avoid biasing the results of the ABI-focused experiments starting at 17:10 UTC. Different configurations of ABI channel 9 and ABI channel 10 observations are then assimilated every 10 min, together with radar reflectivity, from 17:10 to 19:00 UTC. Given the reduced availability of conventional observations in 10 min cycles compared to at the top of the hour, conventional observations are not assimilated in the 10 min cycles to help focus on the impact of different methods of assimilating the ABI observations. Deterministic forecasts are initialized from the ensemble mean analysis every 10 min starting at 18:00 UTC. Rather than mimicking an operational DA and forecast system configuration, this configuration is chosen to focus on and reveal the impacts of assimilating ABI channels 9 and 10 with additive inflation and adaptive observation error.

The DA system is configured with a horizontal covariance localization cut-off radius of 300 km for conventional observations and 15 km for both ABI radiance and radar reflectivity observations, using the Gaspari and Cohn (1999) localization function. Vertical covariance localization is 1.1 in units of the natural logarithm of pressure for all observation types. For the purpose of localization, the heights of the ABI radiances are set to the height of the peak in the model prior weighting function while the radar reflectivity data are already on height levels in the MRMS data set. Posterior covariance inflation is applied using the Relaxation to Prior Spread (Whitaker & Hamill, 2012) with a factor of 0.95. This factor is consistent with the value used in Whitaker and

Table 1
Summary of Experiments

Experiment	Add. Infl.	dBZ	Ch. 9	Ch. 10	Obs. error	BG ensemble
Radaronly	N	Y	N	N		
Ch10	N	Y	N	Y	1 K	
Ch10_addn	Y	Y	N	Y	1 K	
Ch10_addn_obserr	Y	Y	N	Y	Adaptive	
Ch9_addn_obserr	Y	Y	Y	N	Adaptive	
Ch9ch10_addn_obserr	Y	Y	Y	Y	Adaptive	
Ch9_addn_obserr_1750bg	Y	Y	Y	N	Adaptive	*Ch10_addn_obserr*
Ch10_addn_obserr_1750bg	Y	Y	N	Y	Adaptive	*Ch9_addn_obserr*

Note. Columns (from left to right) indicate the experiment name, whether additive inflation is applied, whether radar reflectivity is assimilated, whether ABI channel 9 is assimilated, whether ABI channel 10 is assimilated, ABI observation error, and source of 17:50 UTC background ensemble if taken from a different experiment. All experiments also assimilated NEXRAD reflectivity observations with 5 dBZ observation error.

Hamill (2012) and other studies such as Gasperoni et al. (2020). Default observation error standard deviation of 5 dBZ for reflectivity and 1 K for ABI radiance is used for the baseline experiments.

2.4. Assimilated Observations

Pre-processing of the radiance data includes parallax correction, partial cloudy pixel removal, and thinning. The parallax correction follows Jones et al. (2020) and C. P. Wang and Huang (2014), using the ABI L2 cloud height product. The ABI level 2 cloud fraction product is used to identify and remove partial cloudy pixels as those with cloud fraction greater than 5% and less than 95%. While partial cloudy pixel removal affects very few pixels in the 2 km resolution ABI data, it is aimed at preventing the assimilation of features that are not resolvable by the model. The observed radiances are thinned from their native grid spacing of 2 km to a 4 km spacing over the Southern Plains region of interest and to a 12 km spacing over the remainder of the CONUS domain, for the purpose of computational efficiency. While the 12 km thinning is comparable to the 15 km cut-off radius for covariance localization, the frequent 10 min cycling mitigates the potential for sampling noise in the final analysis by allowing the increment information to spread between observations during each subsequent cycle. In the region of interest, the 4 km thinning is much less than the covariance localization cut-off radius. Since very large innovations between the observed and first guess radiance are expected at convective scale resolutions during periods of CI, and do not necessarily indicate bad observations, the innovation-based quality control of radiance observations in GSI is turned off. Manual inspection confirmed that large innovations in the region of interest were caused by meteorologically relevant features rather than anomalous observations of questionable accuracy. Similar relaxation of quality control was also applied for all-sky microwave radiance assimilation (Zhu et al., 2019), although it was not turned off completely in their study due to spuriously large innovations near coastlines which are not a concern for our region of interest or for upper-level water vapor channels. However, it should be noted that there is a trade-off involved in including large innovations because it results in a more non-Gaussian distribution of innovations (e.g., Okamoto et al., 2014). The radiances values are converted to an equivalent BT for assimilation following common practice (e.g., Y. Zhang et al., 2018).

2.5. Experiment Design

A set of experiments is designed to address the goals of this study as described above in Section 1 (Table 1). The ABI radiances are assimilated together with NEXRAD radar reflectivity in all experiments except an experiment only assimilating radar reflectivity, but no ABI radiances (*radaronly*). While the *radaronly* experiment can provide a baseline of comparison for the experiments, the focus of this study is on the different methods of assimilating the ABI observations rather than comparing the ABI and reflectivity assimilation to radar alone which has already been done in other studies (Jones et al., 2020; Y. Zhang et al., 2019, 2018). The experiment assimilating radar reflectivity and ABI channel 10 (*ch10*) is used to evaluate the impacts of the implementation of additive inflation and adaptive observation error (*ch10_addn* and *ch10_addn_obserr*, respectively). The experiment with both additive inflation and adaptive observation error is then used to compare the impacts of assimilating ABI channel 10 (*ch10_addn_obserr*) with assimilating ABI channel 9 (*ch9_addn_obserr*) and both ABI channels 9 and 10 (*ch9ch10_addn_obserr*).

2.6. Adaptive Observation Error

Since the default observation errors in this study of 1 K for radiance and 5 dBZ for reflectivity are at the low end for radiance, and high end for reflectivity, of what other studies have used (e.g., Duda et al., 2019; Jones et al., 2018; Minamide & Zhang, 2017), we also implement an adaptive observation error as a function of the symmetric cloud affect, following Harnisch et al. (2016) and Okamoto et al. (2014) in order to better combine the information from the radar reflectivity and ABI radiance observations in the DA system.

The first step in the Harnisch et al. (2016) method is to quantify the cloud affect on the forecast and observed radiances. This is done by defining a limiting BT, BT_{lim}, that largely separates the cloudy radiances with BT colder than BT_{lim} from the clear air radiances with BT warmer than BT_{lim} for each radiance channel. The BT_{lim} is found by plotting the distribution of the prior radiances of ensemble mean forecasts vs. the clear-sky component of the same radiances. The clear-sky component of radiance is also calculated by CRTM but with cloud and precipitation hydrometeors set to zero. Following Harnisch et al. (2016), the BT_{lim} is identified as the BT where the average difference between the total and clear-sky component of BT begins to deviate from zero on average.

The cloud affect is then defined as the difference of the BT from the clear sky BT_{lim}, if $BT < BT_{lim}$. The cloud affect on forecast (C_f) and observed (C_o) radiances, respectively, is thus $C_f = \max[0, BT_{lim} - BT_f]$ and $C_o = \max[0, BT_{lim} - (BT_o - \beta)]$, where BT_o is the observation BT and BT_f is the BT of the ensemble mean background. The average difference between forecast and observed radiances, β, is removed from BT_o in the calculation of C_o because BT_{lim} is determined using the forecast, rather than observed, radiances. The cloud affect is interpreted as a loose measure of the impact of clouds on causing the BT to be colder than the clear sky limit, BT_{lim}. The symmetric cloud affect, $C = (C_f + C_o)/2$, is interpreted as the average impact of clouds on the forecast and observed radiance at a given pixel. The symmetric cloud affect is greatest when both forecast and observed radiance are strongly affected by cloud and is zero when both forecast and observed radiances are in clear air.

An initial experiment assimilating channel 9 ABI radiance and radar reflectivity with no ABI bias correction during DA was used to collect the statistics needed to determine BT_{lim}. The purpose of assimilating observations in this initial experiment is to remove spurious cloud and provide the initiation of deep convection. Since BT_{lim} depends on the model's own simulated radiances, the same experiment can be used for determining BT_{lim} for both channel 9 and channel 10. Setting the BT threshold to 239 K for channel 9 and 251 K for channel 10 results in ~95% of pixels classified as "clear" having ≤2K of influence from clouds on the simulated BT, while less than 5% of pixels classified as "cloudy" have approximately zero influence from clouds on the simulated BT in the model first guess data from all DA cycles (Figure 4). These BT_{lim} values are then used to calculate the root mean square innovation (RMSI) as a function of C for different ABI radiance channels, with a bin size of 1 K for C (Figure 5; thin black line). Following standard DA terminology, the RMSI for all N samples within a given bin of C is calculated as $\sqrt{\frac{1}{N}\sum_{i=1}^{N}\left(y_i - H_i\left(\overline{x}\right)\right)^2}$, where y is the observed radiance (i.e., BT_o) and $H_i\left(\overline{x}\right)$ is the corresponding forecast radiance (i.e., BT_f) obtained by applying the observation operator to the ensemble mean forecast. Assuming the observation and forecast errors are uncorrelated, this can also be written RMSI $\approx\sqrt{\sigma_o^2 + \sigma_f^2}$, where σ_o^2 is the observation error variance and σ_f^2 is the forecast error variance. If the forecast error variance were known then we could trivially calculate the observation error variance directly using this form of RMSI.

The ensemble variance is often used as an estimate of the forecast error variance (e.g., Desroziers et al., 2005). The validity of this estimate cannot be directly evaluated without a known observation error variance. However, the consistency between forecast error variance and ensemble spread can be improved by removing systematic bias from the forecast because systematic bias contributes to forecast error variance but not ensemble spread. This bias removal is done by subtracting the bias, $B = \overline{\left(y - H\left(\overline{x}\right)\right)}$, within each bin of C (Figure 5; blue line) before calculating a bias-corrected RMSI, $RMSI_{bc}$ (Figure 5; thick black line). The $RMSI_{bc} = \sqrt{\frac{1}{N}\sum_{i=1}^{N}\left(y_i - H\left(\overline{x_i}\right) - B\right)^2} \approx \sqrt{\sigma_o^2 + \sigma_e^2}$, where σ_e^2 is the ensemble variance, is then used to

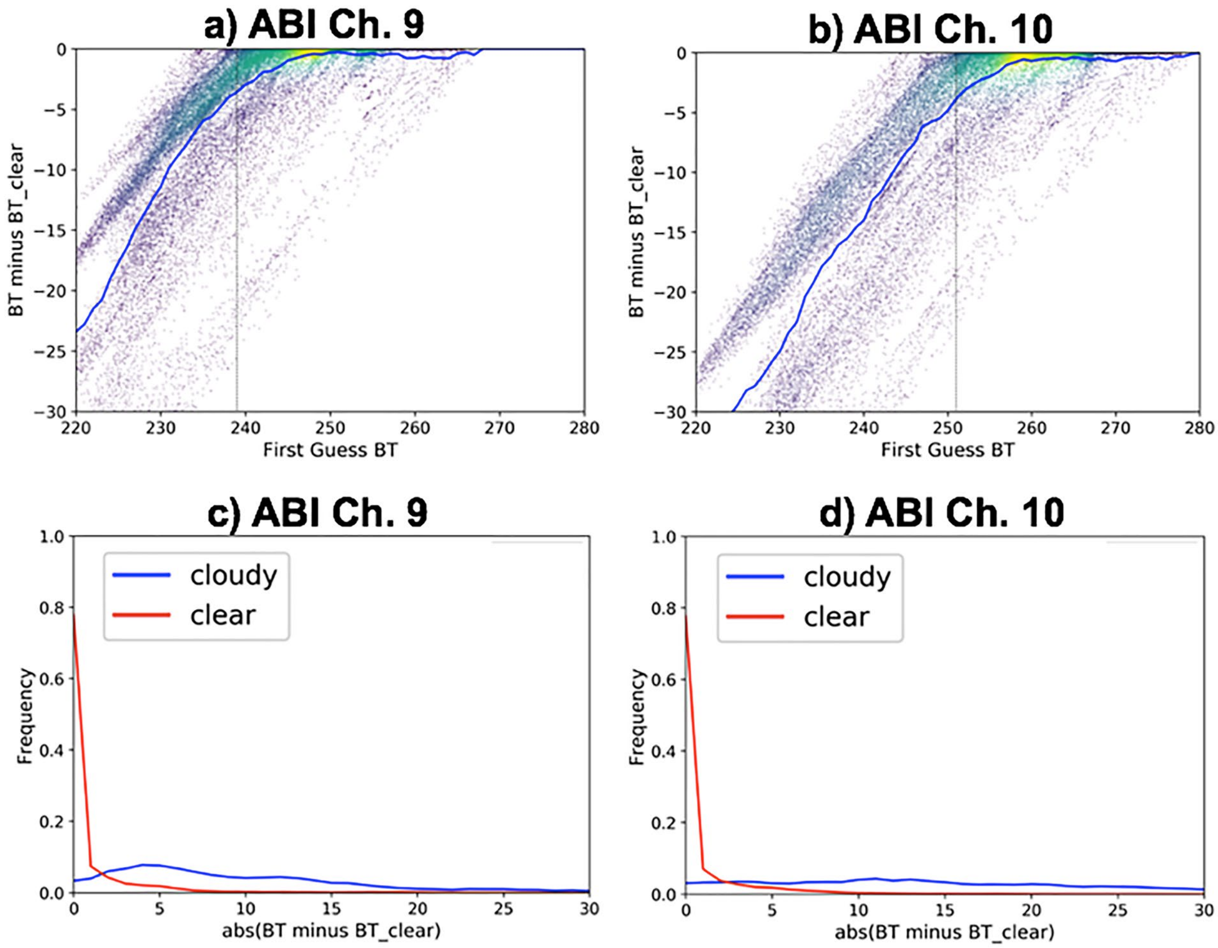

Figure 4. Panels (a and b) are scatterplots (with warmer colors indicating greater density) of the cloud affect on BT (BT minus BT_{clear}) vs. BT, in the ensemble mean prior during an initial experiment with neither bias correction nor adaptive observation error, for (a) ABI channel 9 and (b) ABI channel 10, with the mean value as a function of BT overlaid in blue. Panels (c and d) show the frequency of clear (right of the vertical gray line in (a and b); red lines) and cloudy (left of the vertical gray line in (a and b); blue lines) pixels as a function of cloud affect for (c) ABI channel 9 and (d) ABI channel 10.

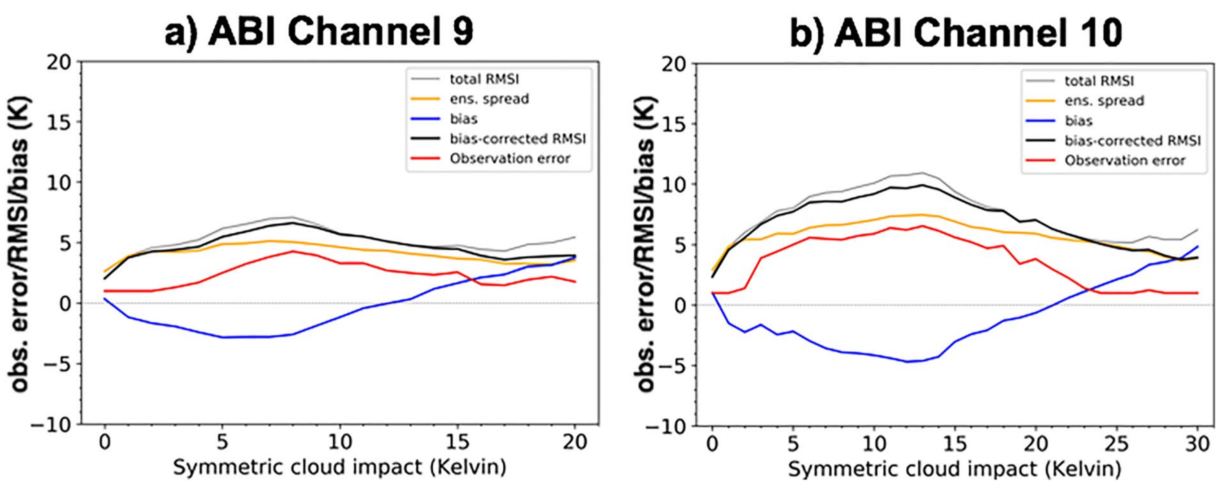

Figure 5. Distributions of bias (blue), root mean square innovation (RMSI) (gray), bias-corrected RMSI (black), ensemble standard deviation (orange) and implied observation error (red) as a function of the symmetric cloud impact for (a) ABI channel 9 and (b) ABI channel 10.

estimate the observation error standard deviation (Figure 5; red line) using the known ensemble standard deviation (Figure 5; orange line). It should be noted that this bias is used only for estimating observation error while a simpler bias correction is applied when assimilating the observations (Section 2.8, below). An additional constraint is added that sets the minimum estimated observation error standard deviation to 1 K. Thus, the net effect of the adaptive observation error is to increase the observation error of the assimilated radiances.

The same observation error estimates shown in Figure 5 are used for all DA cycles in the experiments that include adaptive observation error. Figure 5 (red lines) shows that the adaptive observation error is largest for values of symmetric cloud affect that are neither very large nor very small. This generally corresponds to cloudy observations where the forecast is cloud-free and cloud-free observations where the forecast is cloudy. The former case is more frequently encountered, resulting in the positive bias (blue lines) for bins where the estimated observation error is largest (i.e., >13 K for channel 9 and >21 K for channel 10). Since the ensemble spread (orange lines) is also farthest below the $\mathrm{RMSI_{bc}}$ (black lines) in these bins, the estimated observation error is inflated the most in these bins.

2.7. Additive Inflation

Additive inflation is newly implemented in the GSI-EnKF system for all-sky ABI radiance assimilation as an external step in the DA workflow. Additive inflation has previously been used to generate sufficient ensemble spread to effectively assimilate radar reflectivity observations in locations where robust convection is observed but all ensemble members forecast absent or excessively weak convection in the background forecast (e.g., Dowell & Wicker, 2009; Sobash & Wicker, 2015; Y. Wang & Wang, 2017, 2020). Following these reflectivity DA studies, additive inflation for radiance DA here aims to generate perturbations that stimulate cumulus development in subsequent DA cycles rather than to immediately correct the background error covariances to be consistent with the cloudy radiance assimilation. With this goal in mind, perturbations are added to lower levels of the prior ensemble at locations that are cloud-affected in observations (i.e., Co > 2K) but clear sky in the ensemble mean prior (i.e., Cf ≤ 2K). In particular, random values with a standard deviation of 0.25, 0.25 K, and 0.25 m s^{-1} are applied to each members' background forecast of temperature, dew point, and wind at every model level below 500 hPa. Increasing the standard deviation of the additive noise perturbations did not improve the performance of the additive noise experiments. Following past studies using additive inflation for reflectivity assimilation (e.g., Y. Wang & Wang, 2017, 2020), and based on the spatial scale of cumulus convection, the perturbations have a spatial de-correlation scale of 12 km in the horizontal and 3 km in the vertical directions. It should be noted that while the locations of applying additive inflation are determined using the ABI radiances, the inflated ensemble affects the assimilation of both radiance and reflectivity observations.

2.8. ABI Radiance Bias Correction

For the experiments in this study, a simple offline bias correction is applied separately to cloud-affected and clear-sky observed radiance pixels using the same $\mathrm{BT_{lim}}$ thresholds and initial experiment without bias correction described above. The bias correction is calculated from and applied to the observation innovation, $y - H(x)$ in data assimilation nomenclature. The convention in the remainder of this paper is that bias is reported as the average value of $H(x) - y$, such that a positive value indicates the model first guess is systematically higher than the corresponding observation. Bias in this study is affected by biases in the observations, the forecast model, and the observation operator. Unlike in Section 2.6, where the goal is to remove the bias in each bin of C for the purpose of estimating observation error, the goal here is to remove the overall systematic bias in clear and cloudy regions during assimilation. Pixels where both the background and observation are clear sky (i.e., $\mathrm{BT} > \mathrm{BT_{lim}}$) are used to calculate the bias correction for clear-sky observations and pixels where both background and observation are cloud-affected (i.e., $\mathrm{BT} < \mathrm{BT_{lim}}$) are used to calculate the bias correction for cloud-affected observations. The ensemble mean priors, and corresponding observations, from all 9 DA cycles from 17:10 to 18:30 UTC are used to calculate the bias which is fixed for all DA cycles in the experiments presented below. The resulting bias values in clear air are 3.77 K for channel 9 and 1.86 K for channel 10. In cloud-affected pixels, the biases are 3.90 K for channel 9 and 5.65 K for channel 10. Following Otkin and Potthast (2019), bias is calculated using the

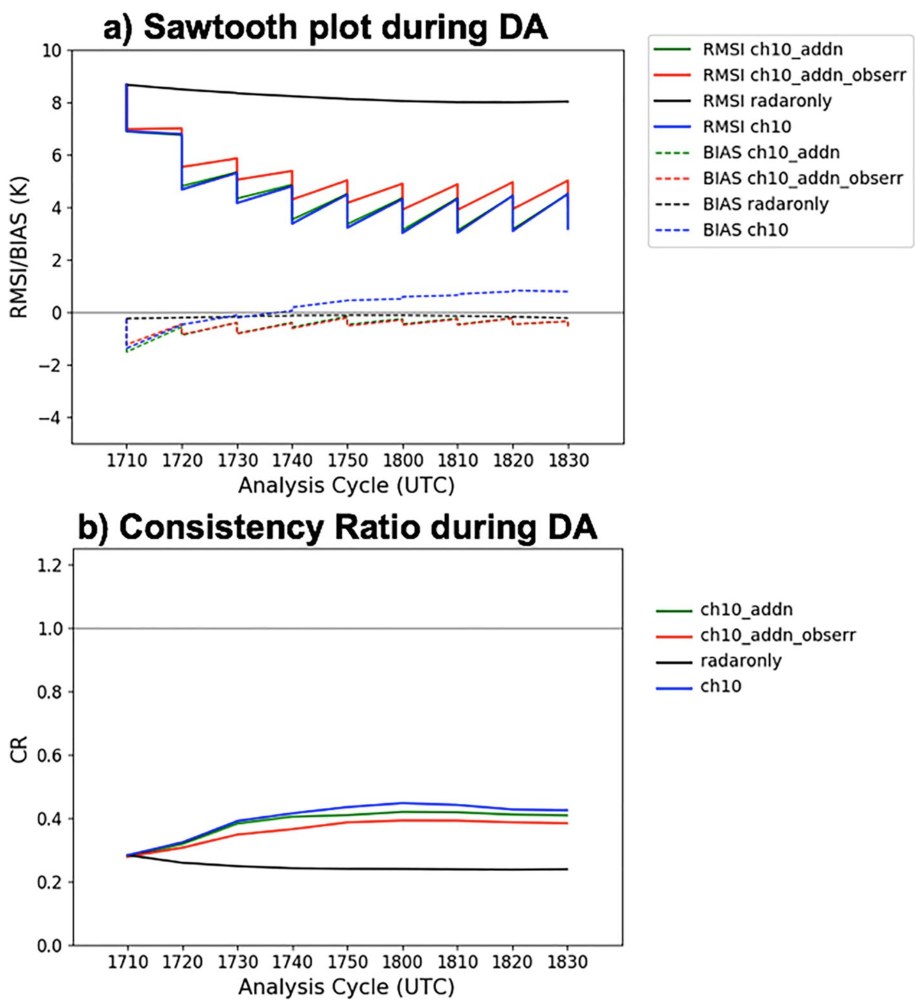

Figure 6. 17:10–18:30 UTC (a) Sawtooth plot of ABI channel 10 brightness temperature root mean square innovation (RMSI; solid) and bias (dashed) during data assimilation for the *radaronly* (black), *ch10* (blue), *ch10_addn* (green), and *ch10_addn_obserr* (red) experiments, and (b) consistency ratio for the same experiments. In panel (a), the line connects the posterior value from each cycle to the prior value in the next cycle.

same case as the bias-corrected innovations are assimilated. While this approach has the advantage of allowing the estimated bias to reflect current conditions, it does have a disadvantage of not truly representing long-term systematic bias. However, Otkin and Potthast (2019) showed that this approach was sufficient for improving DA performance compared to not using bias correction. Although more advanced techniques for bias correction exist (e.g., Zhu et al., 2016), uncertainty remains about the optimal use of such techniques in the context of frequently cycled DA of all-sky ABI radiances during rapidly developing CI events such as this one.

3. Results

3.1. DA Diagnostics

Sawtooth plots calculated over the entire forecast domain for the ABI channel 10 experiments show that the ABI radiance assimilation reduces first guess RMSI by about a factor of 2 (Figure 6a). The RMSI for *ch10_addn_obserr* is generally higher than *ch10* and *ch10_addn*, likely because the adaptive observation error tends to increase the observation error used to assimilate the radiance observations which reduces the analysis fit to those observations. The bias for most experiments is close to zero (Figure 6a; dashed lines), except for ch10 which develops a positive bias of ~1 K in the later DA cycles (Figure 6a; dashed blue line). These biases are explained below by the qualitative inspection of the analyses.

The consistency ratio (CR), calculated following Yussouf et al. (2013) as the ratio of the square root of ensemble variance plus observation error variance (1 K), divided by ensemble mean background RMSI, indicates that all experiments are under-dispersive in terms of ABI radiance (Figure 6b). The same 1 K observation error is used when calculating CR for all experiments to allow comparison among the lines in Figure 6b based on the quality of ensemble spread rather than differences in assumed observation error. The CRs around 0.4 are consistent with some past studies focused on radar DA at convective scales (e.g., Yussouf et al., 2013), but much lower than other studies that have achieved values closer to 1.0 (Wheatley et al., 2015). While the *ch10_addn_obserr* shows even worse CR values than *ch10_addn* and *ch10*, this is due to the larger RMSI of the ABI radiances resulting from the larger observation error during DA causing the analysis increments toward observations to be generally smaller. However, this does not necessarily translate into worse forecasts initialized from the *ch10_addn_obserr* analyses.

The relatively poor CR values in this case can be explained by substantial model first guess errors that were common to all ensemble members and thus contribute to RMSI but not spread. In particular, there is a spurious cloud cover over the region that is not well suppressed by the *radaronly* experiment (e.g., Figure 7a). The stabilizing influence of this cloud cover results in greatly delayed convective initiation for all members in the absence of data assimilation, necessitating the introduction of the additive noise technique (Section 3.2, below).

In contrast to the above quantitative diagnostics, qualitative inspection of analyses can provide a physical basis for understanding analysis differences among the experiments for the supercell features of interest (Figure 7). When ABI radiances are not assimilated (Figures 7a, 7e, and 7i), the northernmost supercell is present in the analysis by 18:30 UTC (Figure 7e, black contours) but there is not a corresponding deep cloud structure associated with it (Figure 7e, shaded). The lack of deep cloud signature associated with the analyzed low-level reflectivity suggests that the storm is not coherently analyzed across all model variables and will still require a spin-up period during the forecast. Compared to the observations (Figures 2e–2h), the *ch10* experiment (Figures 7b, 7f, and 7j) provides a better analysis of the cold cloud tops in both storms of interest, reduces the spurious cloud cover over the region (red contours) and starts to pick up on the reflectivity signature of the northern storm in the 18:10 UTC cycle (black contours). Thus, *ch10* provides a clear subjective improvement in the analyses compared to *radaronly*. The additive inflation experiment (Figures 7c, 7g, and 7k) improves, relative to *ch10*, the magnitude of the cold BT anomalies in the cloud tops (Figures 2e–2h) and improves the analysis of the reflectivity signature of additional cells to the southwest of the northern storm in the 18:30 UTC analysis (Figure 7g). The further addition of the adaptive observation error (Figures 7d, 7h, and 7l) maintains the improved analysis of the cold cloud tops, but does not show a reflectivity signature associated with the southern storm in the 18:30 UTC analysis.

Figure 7 also helps explain the biases seen during DA (Figure 6a; dashed lines). Although *radaronly* showed an overall small bias, this results from two biases that cancel each other out. There is a cold bias resulting from the inability of *radaronly* to fully suppress spurious cloud cover over north Texas and western Oklahoma (Figures 7a, 7e, and 7i). The cold bias is compensated for by a warm bias resulting from the inability of radaronly to quickly add the deep cloud associated with the developing supercells, resulting in little overall bias (Figures 7a, 7e, and 7i). The ch10 experiment does a better job of suppressing the spurious cloud cover but does not have sufficient cold cloud tops in the developing supercells, resulting in the net positive bias (Figures 7b, 7f, and 7j). In contrast, the small bias in ch10_addn and ch10_addn_obserr results from these experiments both suppressing the spurious cloud and adding the cold deep clouds which is physically more realistic (Figures 7c, 7d, 7g, 7h, 7k, and 7l).

While the analysis diagnostics provide a useful first look at whether the different experiments are behaving as expected, the more important impact of the different DA configurations from a practical perspective is the impact on the performance of deterministic forecasts initialized from the ensemble mean analyses which is the focus of the following Section 3.2.

3.2. Impact of Different DA Configurations

Composite reflectivity forecasts initialized from the ensemble mean analyses are first evaluated against the MRMS composite reflectivity using the Fractions Skill Score (N. M. Roberts & Lean, 2008) at 35 dBZ threshold, with different neighborhood radii to determine the spatial scale of useful forecasts in the different experiments

10.1029/2021JD036157

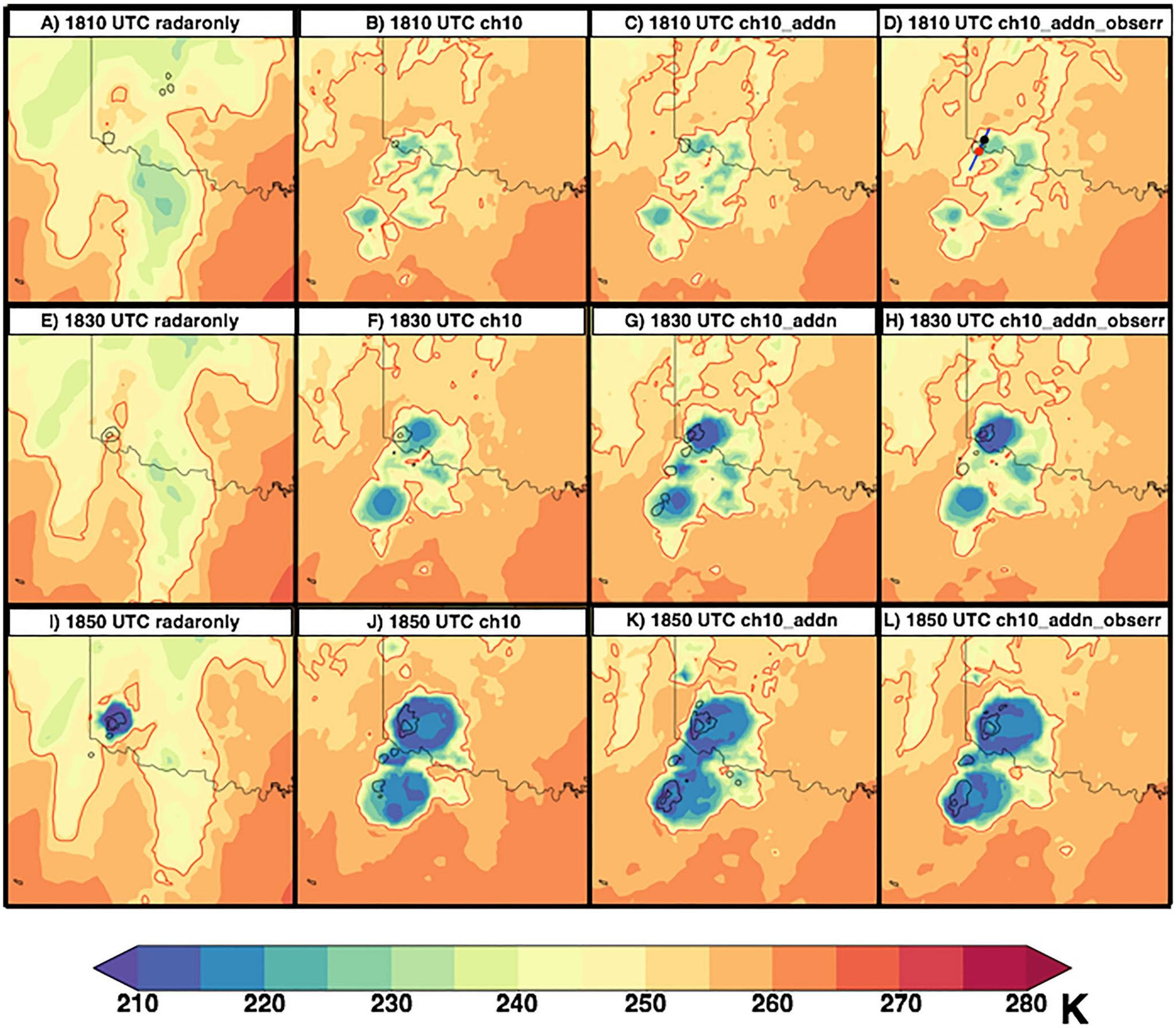

Figure 7. Ensemble mean analysis simulated Advanced Baseline Imager (ABI) channel 10 brightness temperature (shaded), composite reflectivity (black contours every 20 dBZ), and cloud-affected brightness temperature determined using BT_{lim} (red contour) at (first row) 18:10 UTC, (second row) 18:30 UTC and (third row) 18:50 UTC for (first column) *radaronly*, (second column) *ch10*, (third column) *ch10_addn*, and (fourth column) *ch10_addn_obserr*. The blue line in panel (d) indicates the location of the cross-section in Figure 11 and the orange and black dots in panel (d) indicate the locations of two observations discussed in the context of Figure 11.

(Figure 8). The spatial scale of useful forecast is determined following Stratman and Brewster (2017), and is calculated over the verification domain shown in Figure 9. Spatial scales up to 120 km are considered because some forecast times do not have useful skill at any spatial scales due to missing the storms entirely. The reflectivity forecasts generally start to have useful skill starting with the 18:30 UTC initialized forecasts. However, even in the 18:30 UTC initialization, *radaronly* still does not have useful skill (Figure 8a). For later initializations, the useful skill for radaronly generally occurs on larger spatial scales than the other forecasts (Figures 8b and 8c), with the exception of the 19:00 UTC initialization where the improvement of *ch10_addn_obserr* over *radaronly* is short-lived (Figure 8d). For the 18:30 and 18:40 UTC initializations, *ch10_addn_obserr* results in useful skill at even smaller scales than *ch10_addn* (Figures 8a and 8b), but this advantage is lost at 18:50 UTC (Figure 8c) and reversed by 19:00 UTC (Figure 8d). Thus, while the adaptive observation error shows some promise during the early stages of development, further refinement of the method may still be needed when only assimilating one ABI channel. At all initialization times, *ch9ch10_addn_obserr* generally results in useful skill at the smallest

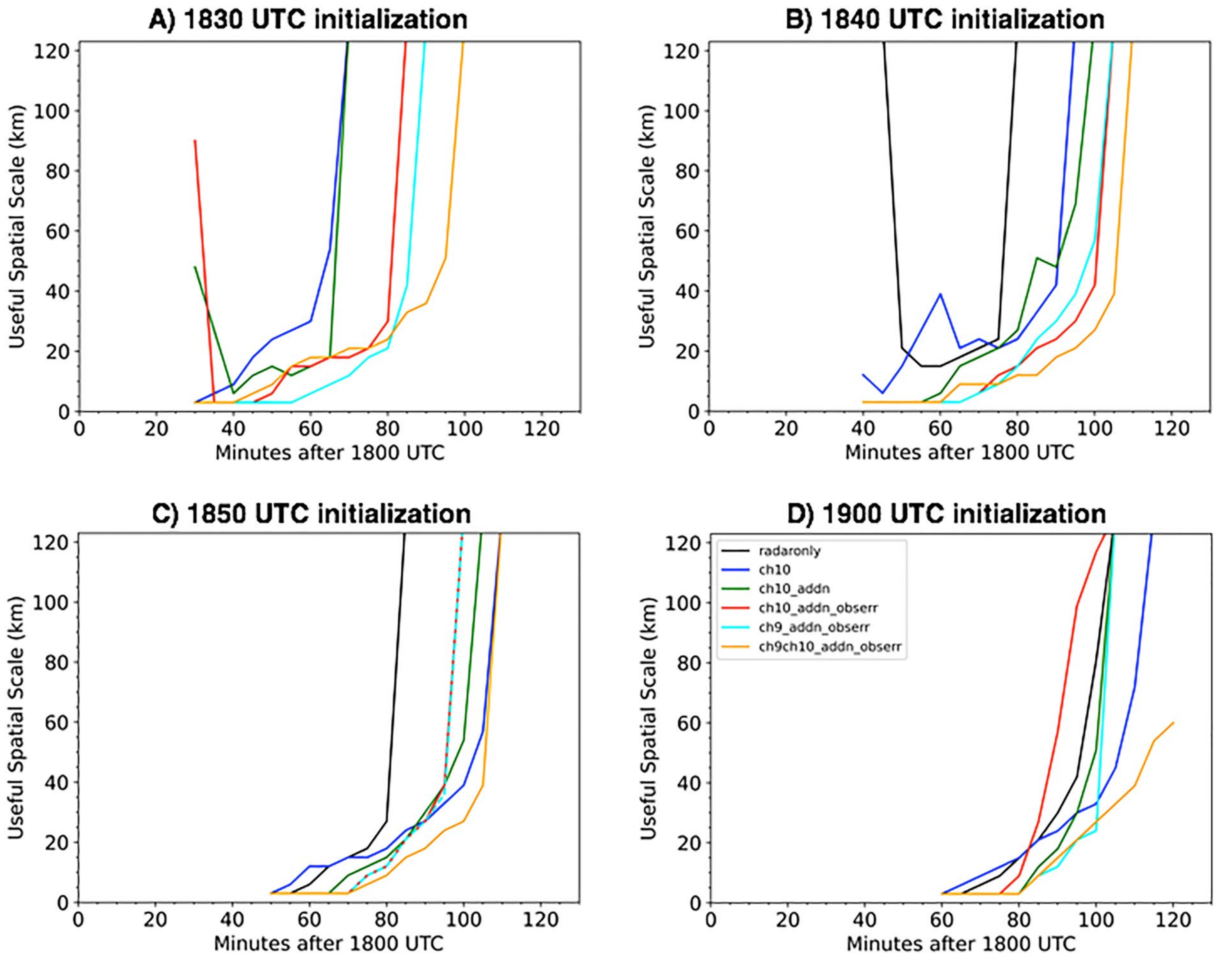

Figure 8. Spatial scale of useful skill according to the Fractions Skill Score of composite reflectivity for forecasts initialized at (a) 18:30 UTC, (b) 18:40 UTC, (c) 18:50 UTC and (d) 19:00 UTC.

spatial scales (Figure 8). All forecasts eventually become unskillful late in the forecast period for two reasons. First, there is elevated convection observed north of the supercells of interest that initiates after the last DA cycle (e.g., as seen in Figure 9c). Second, the forecast supercells begin to weaken late in the forecast period while the observed supercells maintain their intensity. This is likely because late in the forecast period the storm evolution is more strongly influenced by the mesoscale environment than the initialization of the storms. In summary, the addition of channel 10 ABI radiance assimilation to reflectivity assimilation provides limited benefit when additive inflation is not used. The benefit of the additive inflation is lost during the first hour unless adaptive observation error is also used, which increases and extends the benefit of assimilating the channel 10 ABI radiances during the early stages of storm development. This advantage is maintained into later stages of development only if channel 9 is also assimilated.

The time-maximum reflectivity swath is used for subjective evaluation of the forecast supercells because it summarizes the storm evolution over a period of time rather than at a single instant. While elevated convection that formed north of the two supercells of interest after 19:00 UTC (Figures 9a–9c) was missed in all forecasts, the focus of the subjective evaluation is on the two supercells that were responsible for severe reports on this case and formed during the DA period. When channel 10 radiances are assimilated without additive inflation or adaptive observation error (Figures 9g–9i), the first hints of a long-lived storm in the reflectivity swath forecast start to appear with the 18:10 UTC cycle but is not fully developed until the 18:30 UTC cycle. While *ch10* shows improvement over *radaronly* (Figures 9d–9f), the southernmost of the two storms is still not well forecast even with the forecast from the 18:30 UTC cycle (Figure 9h). Although Figure 9h does show what appears to be a second distinct swath of reflectivity, the second swath reflects a weakening and redevelopment of

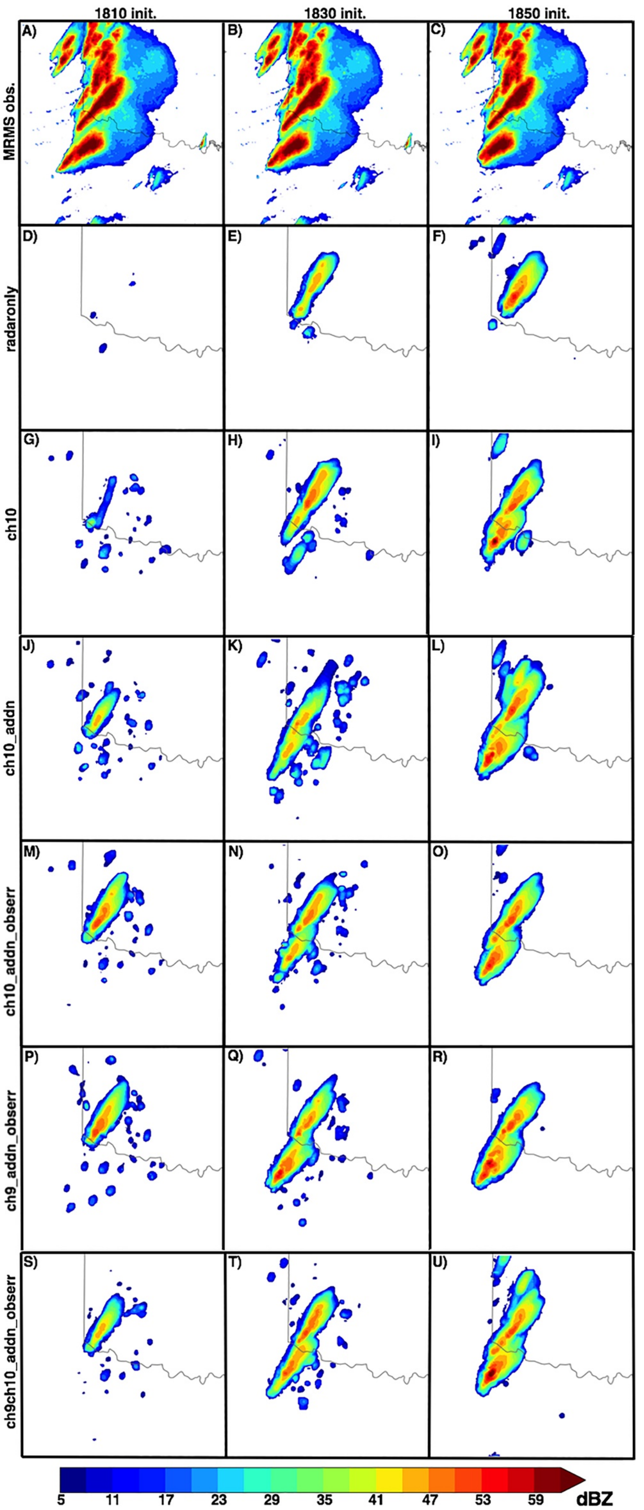

Figure 9. Time-maximum composite reflectivity during the period from the forecast initialization time through 20:00 UTC for (first row) observations, (second row) *radaronly*, (third row) *ch10*, (fourth row) *ch10_addn*, (fifth row) *ch10_addn_obserr,* (sixth row) *ch9_addn_obserr* and (seventh row) *ch9ch10_addn_obserr* experiment forecasts initialized at (first column) 18:10 UTC, (second column) 18:30 UTC and (third column) 18:50 UTC.

the northernmost storm, rather than a correct depiction of the second storm which begins farther south (Figure 9b). The impact of the additive inflation is to allow forecasts of a more robust northernmost storm as early as the 18:10 UTC cycle (Figure 9j) and to pick up on the southernmost storm in the 18:30 UTC cycle (Figure 9k). The additive inflation is particularly helpful at times when all background forecasts are missing the deep clouds that are detected by the ABI radiances. In general, the qualitative evaluation of the forecast reflectivity swaths confirms that the objective differences in forecast skill indeed correspond to physically meaningful differences in the forecast evolution, rather than for example, benefitting from large biases with unrealistic spatial structure.

An example of the additive inflation procedure and impacts is shown in Figure 10. The ability of DA to add an observed storm in the correct location can be seen by considering mid-level vertical velocity as a proxy for updraft strength since the updraft is the driving feature of other variables within the storm. The level near 400 hPa is selected in Figure 10 because the magnitudes of vertical velocity, and vertical velocity increments, are generally maximized near this level. Other levels show similar sign of vertical velocity, and vertical velocity increments, with smaller magnitude. The simulated ABI channel 10 radiance of the ensemble mean first guess at 18:00 UTC (Figure 10a) has several locations that are above BT_{lim} but have observed radiance below BT_{lim} (Figure 10b), and are therefore selected for additive inflation to be applied (Figure 10a; black contours). The region circled in black is of particular interest for improving the assimilation of the southernmost supercell (Figure 10a). A direct impact of the additive inflation is to increase the low-level temperature spread in this region after additive inflation is applied (Figure 10d), compared to before additive inflation is applied (Figure 10c). The inflation does not immediately lead to an improved assimilation of the observed storm, in terms of adding an updraft in the appropriate location at 1800 UTC (Figure 10e). However, an updraft is added in the next assimilation cycle at 18:10 UTC for the *ch10_addn* experiment (Figure 10f), but not the *ch10* experiment without additive inflation (Figure 10h). The difference between the vertical velocity increments at 18:10 UTC in *ch10* and *ch10_addn* demonstrates that the additive inflation is improving the storm spin-up during DA of the all-sky ABI radiances. Figure 10 also reveals a limitation of the additive inflation approach as currently implemented. In particular, the analysis increments are not improved immediately in the 18:00 UTC analysis by the use of the additive inflation. The added inflation requires at least one forecast cycle to spin up the appropriate covariances for adding deep convection to the analysis. This delayed impact is similar to how additive inflation is typically used for radar DA applications (Dowell & Wicker, 2009; Sobash & Wicker, 2015).

The impact on the reflectivity forecast of further adding the adaptive observation error to the ABI observations is mainly to increase the amplitude of the forecast reflectivity swaths in the 18:10 and 18:30 UTC initializations (Figures 9m and 9n) compared to *ch10_addn* (Figures 9j and 9k), suggesting more intense storms in the *ch10_addn_obserr* experiment. The advantage of the adaptive observation error can be understood as providing a better balance between the weight given to the ABI radiance, which detects the early development of a deepening cumulus and the top of the convective anvil thereafter, and the weight given to the radar reflectivity, which detects the lower-level and internal precipitation structure even during the mature storm phase. This difference is illustrated by the influence of two pairs of co-located

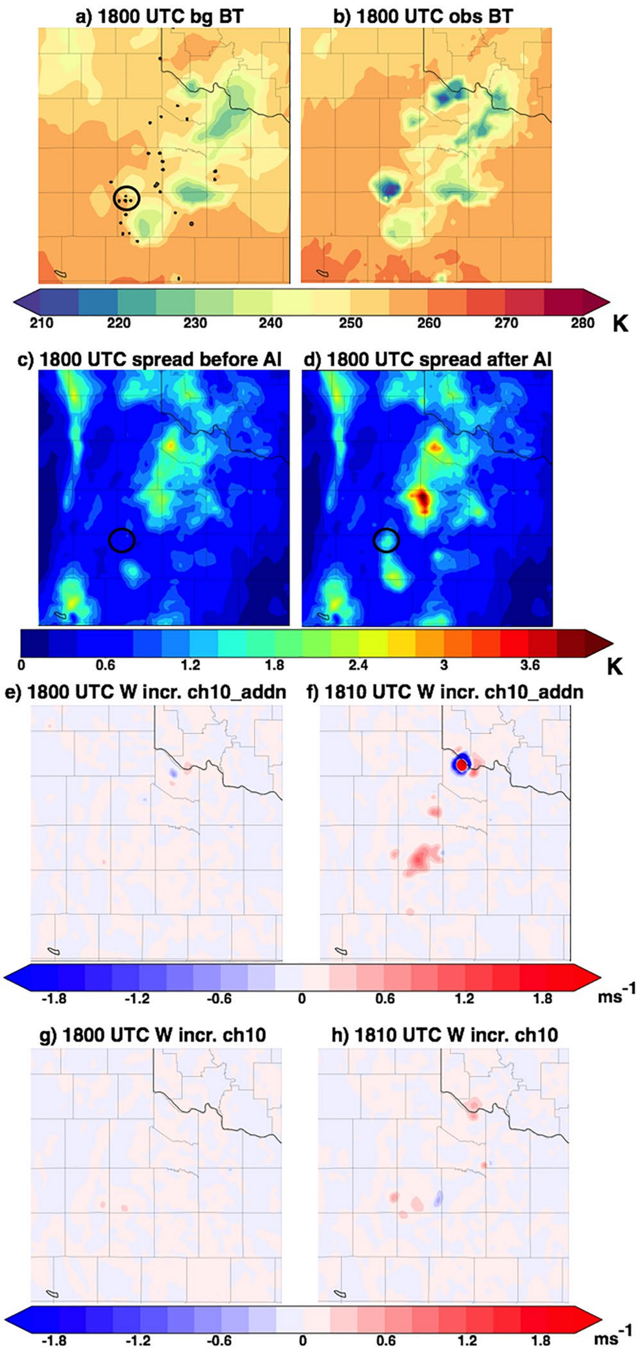

Figure 10. Demonstration of the additive inflation impact, showing (a) 18:00 UTC ensemble mean *ch10_addn* background simulated channel 10 brightness temperature (shaded) and locations where additive inflation is applied (black contours), (b) Advanced Baseline Imager (ABI) observed brightness temperature at 18:00 UTC, *ch10_addn* background ensemble standard deviation of temperature at the first model level at 18:00 UTC (c) before, and (d) after additive inflation is applied. Panels (e–h) show the analysis increment of vertical velocity at model level 21 (~400 hPa) for (e) *ch10_addn* at 18:00 UTC, (f) *ch10_addn* at 18:10 UTC, (g) *ch10* at 18:00 UTC, and (h) *ch10* at 18:10 UTC. Black circles highlight locations emphasized in the text.

reflectivity and radiance observations along the blue line in Figure 7d at the location of the red and black dots in Figure 7d. The cross-section of observed (Figure 11a) vs. *ch10_addn_obserr* ensemble mean background (Figure 11b) reflectivity at 18:10 UTC shows that the background forecast has too-weak and too-shallow reflectivity along the orange line in Figures 11a and 11b and too-strong reflectivity along the black line in Figures 11a and 11b. The channel 10 ABI radiance innovation (i.e., observation minus ensemble mean first-guess) is negative at both locations due to insufficiently cold cloud tops in the convective anvil (Figure 2f vs. Figure 7d). The reflectivity innovation is positive at the orange dot (Figures 11a and 11b) and negative at the black dot (Figures 11a and 11b).

The background error covariance (e.g., Whitaker & Hamill, 2002) between the ensemble priors of reflectivity and radiance at the orange dot and line (Figure 11b), respectively, and the model variables along the cross-section illustrate the different impacts on the analysis of assimilating a radiance or reflectivity observation, using the same background ensemble from *ch10_addn_obserr* at the 18:10 UTC cycle. The covariances in Figures 11c–11f are multiplied by the sign of the innovation (observation minus ensemble mean first-guess) and referred to hereafter simply as the background error covariance. This convention allows Figures 11c–11f to all be interpreted as how the information from the innovation is spread to different model variables by the EnKF. The background error covariance of ensemble priors for the radiance observation (Figure 11c; orange line) suggests that upper-level moistening and destabilization (i.e., cooling above warming) would result from assimilating this observation. The background error covariance of ensemble priors for the reflectivity observation at 450 hPa (Figure 11d; orange dot) suggests that the addition of mid-level moisture and cloud condensate, together with low-level warming, would result from assimilating this observation. Thus, the assimilation of reflectivity and radiance at this location help each other to make the column more favorable for storm strengthening at this location.

The background error covariance of ensemble priors for the radiance observation at the black line (Figure 11e) indicates upper-level moistening and destabilization at this location would result from assimilating this observation as well. In contrast, the background error covariance of ensemble priors for the reflectivity observation at 600 hPa (Figure 11f; black dot) in this location where the background storm is too strong indicates mid-level cooling and drying would result from assimilation of this reflectivity observation. Thus, in the second location the reflectivity observation is impacting the analysis in a more physically intuitive way than the radiance observation. The discrepancy is due to the fact that the cloud top radiance signal provides little information about the convective scale variability at lower levels as the anvil cloud begins to expand. The reflectivity observations are better suited than the radiance observations to constrain the internal storm structure as the storm matures. The adaptively increased radiance observation error (Figure 5) can allow the DA system to place more weight on the information about these storm structure details provided by the reflectivity observations, which have fixed observation errors in all experiments, in such situations.

3.3. Impact of Different ABI Channels

Experiments were also conducted using the ABI channel 9 radiances (Figures 9p–9r) instead of channel 10 (Figures 9m–9o). The main impact of switching to channel 9 on the forecast reflectivity is to pick up on the

10.1029/2021JD036157

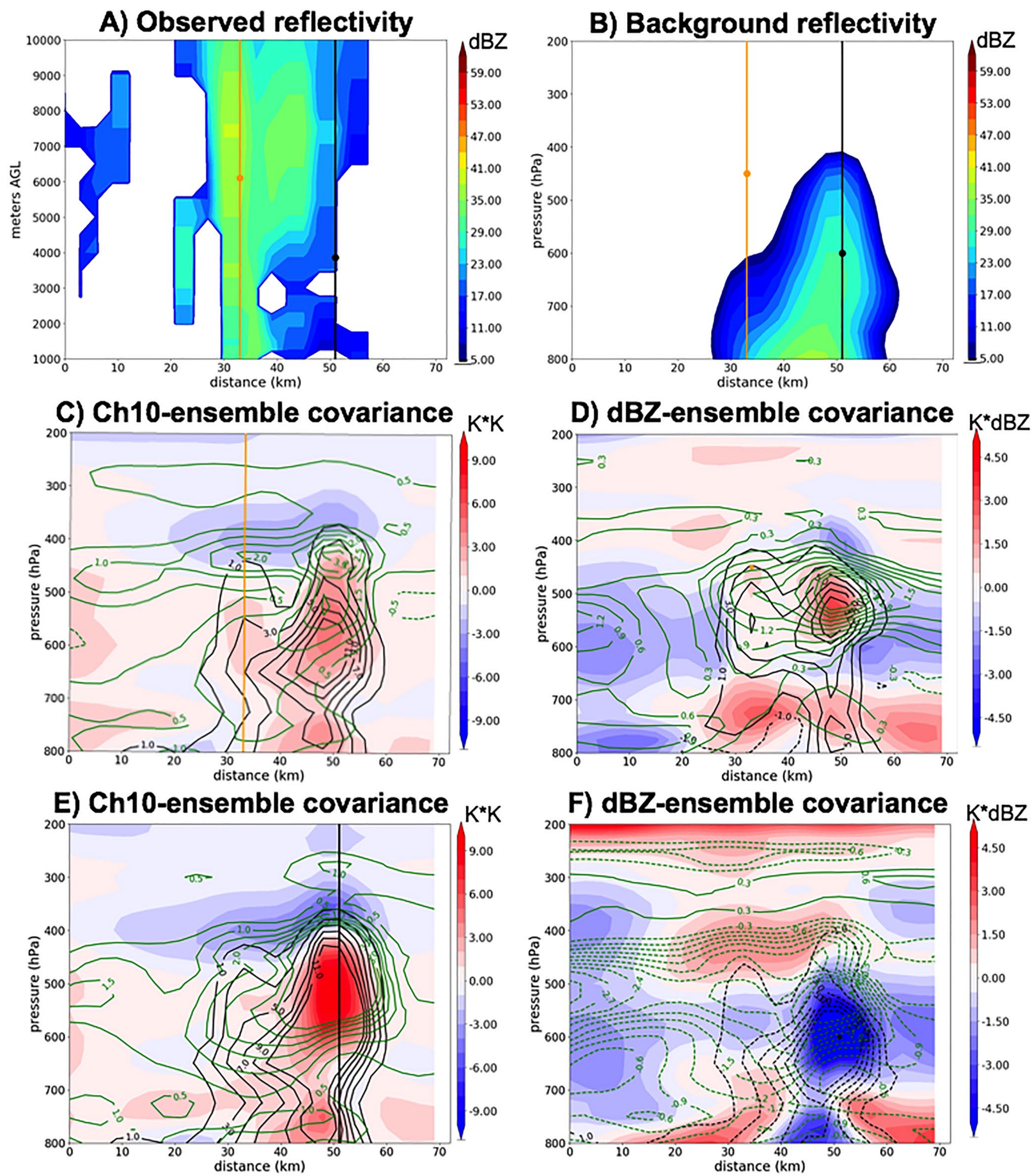

Figure 11. Panels (a and b) show cross-sections of reflectivity along the blue line in Figure 7d for (a) Multi-Radar Multi-Sensor (MRMS) observations and (b) ensemble mean background in the 18:10 UTC cycle of the *ch10_addn_obserr* experiment. Panels (c and d) are corresponding cross-sections of the background error covariance between temperature (shaded; K*K and dBZ*K, respectively), water vapor mixing ratio (green; K g kg^{-1} and dBZ g kg^{-1}, respectively, with zero lines suppressed) and total cloud condensate (black; K g kg^{-1} and dBZ g kg^{-}, respectively, with zero lines suppressed) and the ensemble priors of the (c) radiance observation at the location of the vertical orange line and (d) reflectivity observation at the location of the orange dot. Panels (e and f) are the same as in (c and d), except using the (e) radiance observation at the vertical black line and (f) reflectivity observation at the black dot.

southernmost storm one cycle (10 min) earlier (not shown) and producing a stronger reflectivity swath in the southern storm of the 18:30 UTC initialization (Figure 9q). Assimilating both channels (Figures 9s–9u) generally results in higher reflectivity values through the entire swath of the storms in the 18:30 and 18:50 UTC initializations, consistent with the improved skill for *ch9ch10_addn_obserr* seen in Figure 8.

The improvement when assimilating both ABI channels appears related to the differences in how channel 9 and channel 10 observe the larger-scale environment in which the storms develop. It was found that the analysis increments within the storms as they first begin to initiate were qualitatively similar for channel 9 and channel 10 (not shown). However, the ensemble members start to initiate the southernmost storm in the background ensemble forecasts about 10 min earlier in the *ch9_addn_obserr* experiment than the *ch10_addn_obserr* experiment, contributing to a 10 min forecast lead time improvement. This forecast improvement can be attributed to the difference between the experiments in the analysis of the larger-scale features in clear air that are supporting the initiation of the storms (Figures 1d–1f). In particular, the approach of a mesoscale upper-level vorticity maximum would be expected to contribute to the weakening of convective inhibition along and ahead of the dryline where the storm initiates as a result of the associated differential cyclonic vorticity advection.

Figure 12a shows the difference in ensemble mean background forecast relative humidity at 350 hPa in *ch9_addn_obserr* from *ch10_addn_obserr*. Figures 1d–1f suggested the possibility that features in the upper-level humidity field may be dynamically linked to the structure of mesoscale vorticity maxima embedded in the synoptic-scale trough. This suggestion is further confirmed by the correlation between 350 hPa relative humidity and vorticity in the 18:00 UTC background ensemble forecasts in the *ch10_addn_obserr* experiment (Figure 12b). These correlation structures are similar from 300 to 400 hPa and therefore only shown at the 350 hPa level. Figure 12c confirms that the difference in 350 hPa vorticity between *ch9_addn_obserr* and *ch10_addn_obserr* at 18:00 UTC includes enhanced vorticity (Figure 12c green circle) immediately upstream of the development location of the southern supercell in the *ch9_addn_obserr* experiment. Thus, the impact of assimilating ABI channel 9 rather than channel 10 may have been due to the greater sensitivity to upper-level features in the humidity field that result in changes to the vorticity field consistent with enhancing the cyclonic vorticity advection increasing with height in the region of CI. Although the channel 9 peak weighting function is at ∼400 hPa, there is also substantial sensitivity at least 100 hPa above and below this level (Schmit et al., 2017)

The hypothesis that the forecast differences between *ch9_addn_obserr* and *ch10_addn_obserr* result from the differences in the larger-scale analyses before the storms initiate is evaluated with two additional diagnostic experiments, referred to as *ch9_addn_obserr_1750bg* and *ch10_addn_obserr_1750bg*. The experiments are the same as *ch9_addn_obserr* and *ch10_addn_obserr*, except that the background ensemble forecasts are taken from the *ch10_addn_obserr* and *ch9_addn_obserr* experiments, respectively, before the DA update in the 17:50 UTC cycle. In other words, the background ensemble forecasts are swapped before the 1750 DA update, which is before the two supercells developed. The purpose of this diagnostic experiment is to test whether the different analysis increments from channel 9 and channel 10 in the larger-scale environment before storms develop is the cause of the different performance of forecasts initialized from the analyses in later cycles. The result of this experiment (Figure 13) confirms that the differences in how the larger-scale environment prior to 17:50 UTC is analyzed causes the differences in forecasts initialized at later cycles (e.g., Figure 13). One such difference was shown to be related to an upper-level vorticity maximum, which is correlated with upper-level moisture that ABI radiances are sensitive to, and likely played a role in the CI. This difference can be explained by the fact that the channel 9 weighting function has greater sensitivity to the upper troposphere and thus has more impact on the analyzed shortwave than channel 10.

4. Summary and Discussion

This study aims to contribute to the understanding of the impacts of different methods of assimilating ABI all-sky IR radiance observations together with radar reflectivity for short-term forecasts of rapidly evolving high-impact convective-scale features. In particular, we use a case study of forecasts initialized during the rapid development of two long-track severe supercells that organized and became severe within tens of minutes of the first appearance of deepening cumulus development. Such a case is expected to reveal the benefits of assimilating the ABI radiances because of the high space and time resolution of the ABI. First, experiments aimed at understanding the impact of additive inflation and adaptive observation error implementations within the GSI-EnKF system

10.1029/2021JD036157

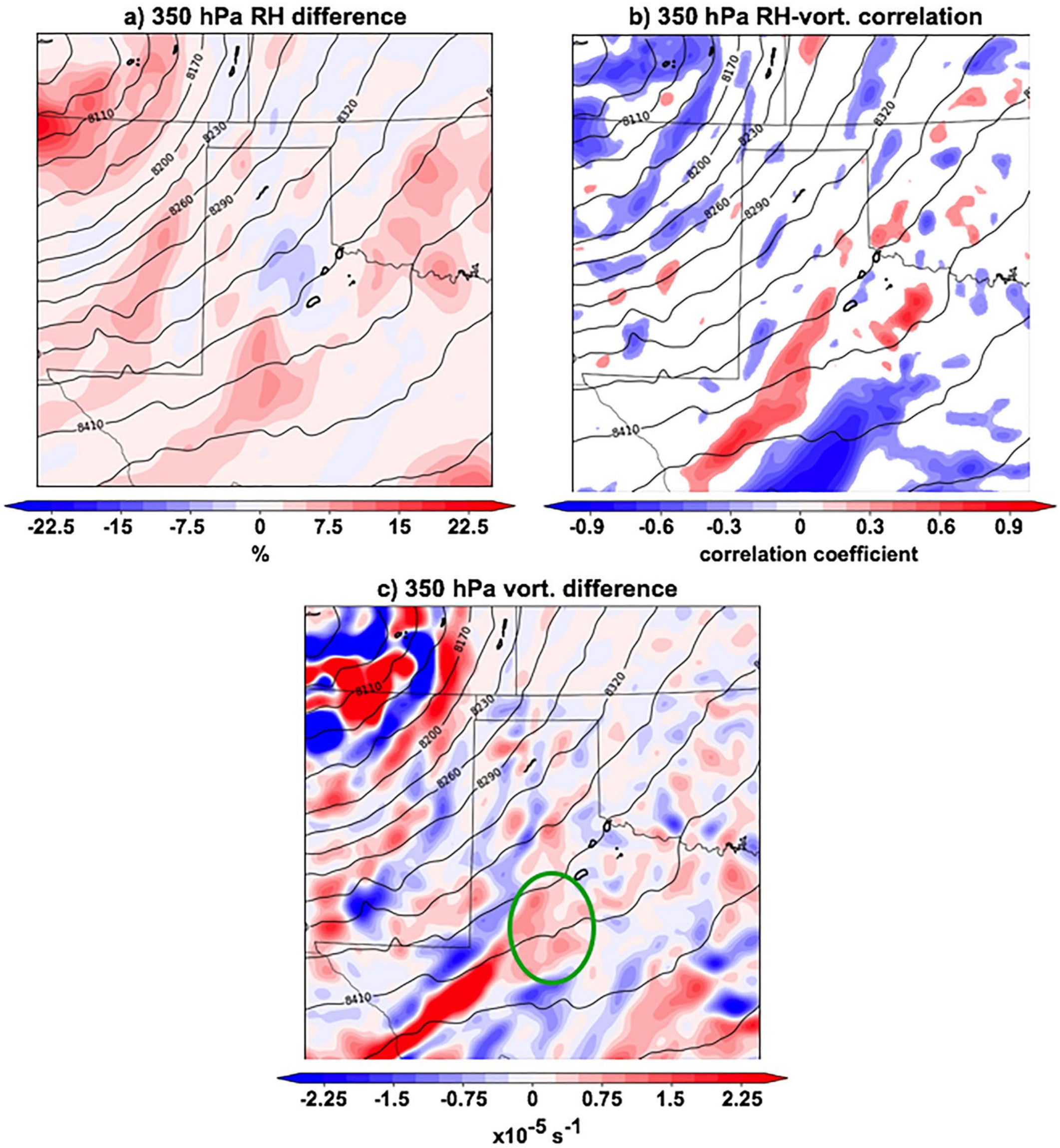

Figure 12. (a) 18:00 UTC ensemble mean background difference of *ch9_addn_obserr* minus ch10_addn_obserr relative humidity (%) at 350 hPa. (b) ch10_addn_obserr background ensemble correlation between relative humidity and absolute vorticity perturbations. (c) as in (a) except for absolute vorticity (x10^{-5} s^{-1}). All difference values are smoothed with Gaussian smoother with spatial scale of 15 km and Multi-Radar Multi-Sensor (MRMS) composite reflectivity (thick black contours every 20 dBZ) at 180:0 UTC is overlaid on all panels. 500 hPa geopotential height contours (thin black) are also overlaid. Correlation in panel (b) is only plotted where the magnitude is statistically significant at the 90% confidence level.

are conducted for the assimilation of the middle-troposphere (~625 hPa) water vapor sensitive channel 10 (7.3 micron wavelength) together with radar reflectivity observations. Second, experiments with additive inflation and adaptive observation error are conducted to compare the impacts of channel 10 to the upper-troposphere (~400 hPa) water vapor channel 9 (6.9 micron wavelength), and both channels together.

Experiments revealed that the additive inflation improved deterministic forecasts initialized from the ensemble mean analysis. In particular, the northernmost storm gained about 20 min of forecast lead time from the additive inflation and the southernmost storm was correctly forecast in the last (18:30 UTC) cycle only when the additive inflation was used. In cases where the cloud was missing from all ensemble members, the impact of the additive inflation was to help trigger deep cumulus development in the background forecast ensemble as soon as the ABI radiance indicated such cloud to be present. The impact of the adaptive observation error was

10.1029/2021JD036157

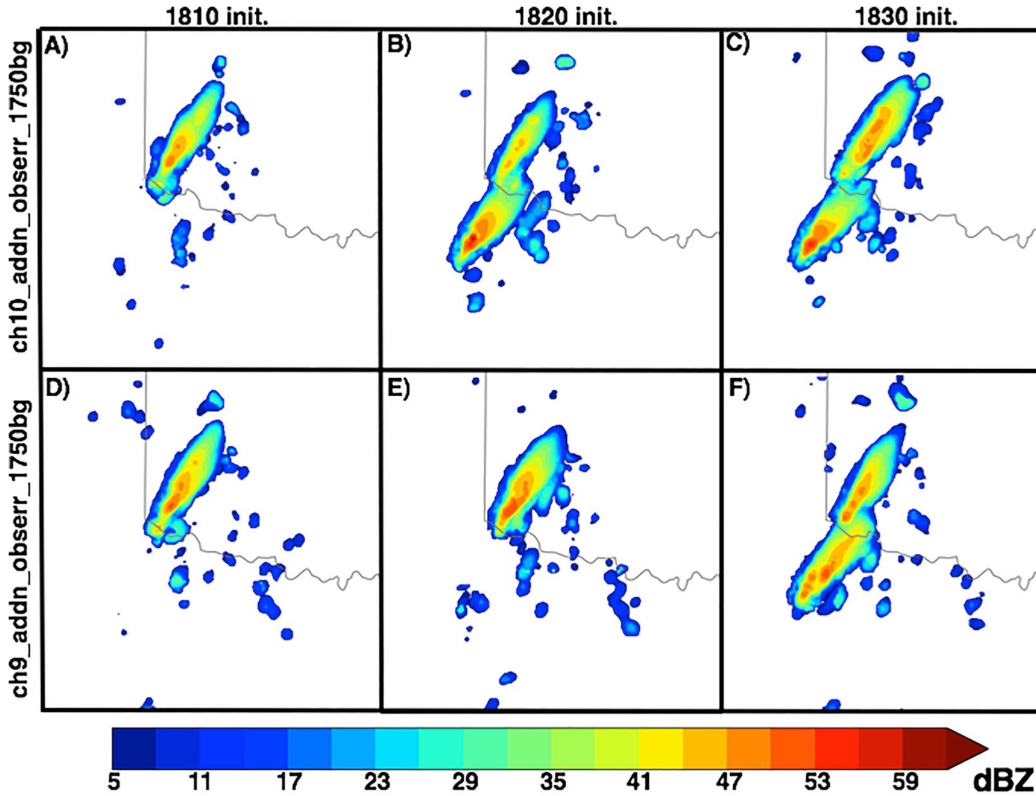

Figure 13. As in Figure 9, except for (a–c) *ch9_addn_obserr_1750bg* and (d–f) *ch10_addn_obserr_1750bg* in (a, d) 18:10 UTC, (b, e) 18:20 UTC and (c, f) 18:30 UTC initializations.

to strengthen the forecast storms, and increase the forecast of the persistent rotating updrafts. This impact of adaptively increasing radiance observation error likely occurs because the ABI radiance was most helpful early in the CI process, but as the storms begin to mature, the benefit of the reflectivity observations detecting details of the internal storm structure becomes relatively more important. The adaptive observation error allowed the analysis increment to give relatively more weight to the reflectivity observations as the storm matured and the cloud anvil spread out, while also benefiting from the increased lead time provided by the ABI radiances during earlier stages of initiation. In this way, the adaptive observation error helped ensure that the all-sky radiance and radar reflectivity were assimilated harmoniously.

To the authors' knowledge, this study is the first to directly compare the impacts of different ABI water vapor channels for the assimilation and short-term forecasting of rapidly developing convective storms. The experiments revealed that the southern storm gained about 10 min of forecast lead time from assimilating channel 9 instead of channel 10. The slight improvement resulting from assimilating the channel 9 radiances is attributed to its better ability to constrain the structure of an upper-troposphere shortwave disturbance that likely contributed to the CI. The best forecast performance was achieved when assimilating both channels 9 and 10, despite the likelihood that their observation errors are at least somewhat correlated. Methods of estimating and fully accounting for correlated observation errors among different assimilated radiance channels for all-sky convective scale DA should still be explored in future work. However, in this case, we find that any observation error correlations do not eliminate the advantage of assimilating both channels 9 and 10 together.

This investigation of a single case study allows for qualitative understanding of how the additive inflation and adaptive observation error, as well as assimilation of the two different ABI channels, can affect short-term forecasts of rapidly developing supercells. However, systematic investigation of a large number of cases is still needed to determine the extent to which this particular case is representative of other cases of rapidly developing supercells. Furthermore, case studies and systematic investigation of other convective systems (e.g., mesoscale convective systems) are needed to determine whether similar impacts are seen for systems with different dynamics and characteristics. Systematic evaluation across many cases is still needed to quantify forecast advantages of these DA techniques and determine optimal DA configurations. Other satellite observations besides ABI are not assimilated in the present study in order to focus specifically on techniques for assimilating the high-resolution and temporally continuous all-sky ABI radiances. Future work should also include all satellite data currently assimilated in operational systems to quantify the incremental advantage of these optimized techniques for assimilating all-sky ABI water vapor channels at convective scales.

The focus of this study is on the ABI radiance DA, rather than the reflectivity DA which has been the focus of other papers (e.g., Dowell & Wicker, 2009; Sobash & Wicker, 2015). It is likely that even further forecast improvements are still possible by further improving the radar DA configuration as well. Further forecast improvements are also expected to result from optimizing the all-sky radiance bias correction procedure, implementing an appropriate static background error covariance model that can be used to generate random perturbations with appropriate convective scale balance in the additive inflation to reduce the spin-up time for the background error covariance structures in the ensemble (Y. Wang & Wang, 2021), and optimizing the microphysics parameterization together with its own radiative transfer model parameters. These aspects will be investigated in future studies. Given the generally low ensemble spread in this case (Figure 6b), future work should also investigate the use of techniques such as multi-physics data assimilation ensemble, stochastic physics, or stochastic models in the context of ABI all-sky assimilation. This is particularly important in the context of adaptive observation error which uses the ensemble spread to approximate forecast uncertainty. While the deterministic forecasts initialized from the ensemble mean analyses are a proxy for the analysis quality in this study, evaluation and optimization of the ensemble forecasts initialized by the analysis ensemble is another worthwhile endeavor that is also left for future study.

Data Availability Statement

The WRF software (WRF-ARW, 2017) used in this study is available at https://www2.mmm.ucar.edu/wrf/users/download/get_sources.html, thanks to the National Center for Atmospheric Research (NCAR). The global model ensemble forecasts (NOAA, 2017) used for initial and lateral boundary conditions are available at https://www.ncdc.noaa.gov/data-access/model-data/model-datasets/global-ensemble-forecast-system-gefs, thanks to the National Center for Environmental Prediction (NCEP). The ABI radiance observations (GOES-R, 2017) are available at https://www.ncdc.noaa.gov/airs-web/search), thanks to NCEP. The GSI-EnKF software (GSI-ENKF, 2018) is available at https://dtcenter.org/community-code/gridpoint-statistical-interpolation-gsi, thanks to the developmental testbed center of NCAR.

Acknowledgments

The work is primarily supported by NA16OAR4320115. This work used the Extreme Science and Engineering Discovery Environment (XSEDE), which is supported by National Science Foundation Grant No. ACI-1053575. Computing for this project was also performed at the OU Supercomputing Center for Education & Research (OSCER) at the University of Oklahoma (OU). The authors are grateful to Jason Otkin and Steve Wanzong for providing the level 2 ABI radiance products, and to Yanqiu Zhu, Xiaoyan Zhang, and Krishnamoorthy Chandramouli during the development of ABI all-sky radiance assimilation in GSI. The manuscript was much improved thanks to the suggestions of three anonymous reviewers.

References

Bedka, M. K., & Khlopenkov, K. (2016). A probabilistic multispectral pattern recognition method for detection of overshooting cloud tops using passive satellite imager observations. *Journal of Applied Meteorology and Climatology*, *55*, 1983–2005. https://doi.org/10.1175/JAMC-D-15-0249.1

Benjamin, S. G., Dévényi, D., Weygandt, S. S., Brundage, K. J., Brown, J. M., Grell, G. A., et al. (2004). An hourly assimilation-forecast cycle: The RUC. *Monthly Weather Review*, *132*, 495–518. https://doi.org/10.1175/1520-0493(2004)132<0495:AHACTR>2.0.CO;2

Cintineo, R. M., Otkin, J. A., Jones, T. A., Koch, S., & Stensrud, D. J. (2016). Assimilation of synthetic GOES-R ABI infrared brightness temperatures and WSR-88D radar observations in a high-resolution OSSE. *Monthly Weather Review*, *144*, 3159–3180. https://doi.org/10.1175/MWR-D-15-0366.1

Desroziers, G., Berre, L., Chapnik, B., & Poli, P. (2005). Diagnosis of observation, background, and analysis-error statistics in observation space. *Quarterly Journal of the Royal Meteorological Society*, *131*, 3385–3396. https://doi.org/10.1256/qj.05.108

Dowell, D. C., & Wicker, L. J. (2009). Additive noise for storm-scale ensemble data assimilation. *Journal of Atmospheric and Oceanic Technology*, *26*, 911–927. https://doi.org/10.1175/2008JTECHA1156.1

Duda, J. D., Wang, X., Wang, Y., & Carley, J. R. (2019). Comparing the assimilation of radar reflectivity using the direct GSI-based Ensemble-Variational (EnVar) and indirect cloud analysis methods in convection-allowing forecasts over the continental United States. *Monthly Weather Review*, *147*, 1655–1678. https://doi.org/10.1175/MWR-D-18-0171.1

Gaspari, G., & Cohn, S. E. (1999). Construction of correlation functions in two and three dimensions. *Quarterly Journal of the Royal Meteorological Society*, *125*, 723–757. https://doi.org/10.1002/qj.49712555417

Gasperoni, N. A., Wang, X., & Wang, Y. (2020). A comparison of methods to sample model errors for convection-allowing ensemble forecasts in the setting of multiscale initial conditions produced by the GSI-based EnVar assimilation system. *Monthly Weather Review*, *148*, 1177–1203. https://doi.org/10.1175/MWR-D-19-0124.1

Geer, A. J. (2019). Correlated observation error models for assimilating all-sky infrared radiances. *Atmospheric Measurement Techniques*, *12*, 3629–3657. https://doi.org/10.5194/amt-12-3629-2019

Geer, A. J., & Bauer, P. (2011). Observation errors in all-sky data assimilation. *Quarterly Journal of the Royal Meteorological Society*, *137*, 2024–2037. https://doi.org/10.1002/qj.830

GOES-R Calibration Working Group and GOES-R Series Program. (2017). NOAA GOES-R Series Advanced Baseline Imager (ABI) Level 1b Radiances. [Dataset]. NOAA National Centers for Environmental Information. https://doi.org/10.7289/V5BV7DSR

GSI-ENKF. (2018). Gridpoint Statistical Interpolation and Ensemble Kalman Filter. Version 1.3. [Software]. GSI-ENKF. Retrieved from https://github.com/NOAA-EMC/GSI

Han, Y., van Delst, P., Liu, Q., Weng, F., Yan, B., Treadon, R., & Derber, J. (2006). *Community Radiative Transfer Model (CRTM): Version 1, NOAA technical report* (p. 122). NOAA.

Harnisch, F., Weissmann, M., M., & Perianez, A. (2016). Error model for the assimilation of cloud-affected infrared satellite observations in an ensemble data assimilation system. *Quarterly Journal of the Royal Meteorological Society*, *142*, 1797–1808. https://doi.org/10.1002/qj.2776

Honda, T., Miyoshi, T., Lien, G.-Y., Nishizawa, S., Yoshida, R., Adachi, S. A., et al. (2018). Assimilating all-sky Himawari-8 infrared radiances: A case of Typhoon Soudelor (2015). *Monthly Weather Review*, *146*, 213–229. https://doi.org/10.1175/MWR-D-16-0357.1

Hutt, A., Schraff, C., Anlauf, H., Bach, L., Baldauf, M., Bauernschubert, E., et al. (2020). Assimilation of SEVIRI water vapor channels with an ensemble Kalman filter on the convective scale. *Frontiers of Earth Science*, *8*, 70. https://doi.org/10.3389/feart.2020.00070

Johnson, A., Wang, X., Carley, J. R., Wicker, L. J., & Karstens, C. (2015). A comparison of multiscale GSI-based EnKF and 3DVar data assimilation using radar and conventional observations for midlatitude convective-scale precipitation forecasts. *Monthly Weather Review*, *143*, 3087–3108. https://doi.org/10.1175/MWR-D-14-00345.1

Jones, T. A., Otkin, J. A., Stensrud, D. J., & Knopfmeier, K. (2013). Assimilation of satellite infrared radiances and Doppler radar observations during a cool season observing system simulation experiment. *Monthly Weather Review*, *141*, 3273–3299. https://doi.org/10.1175/MWR-D-12-00267.1

Jones, T. A., Otkin, J. A., Stensrud, D. J., & Knopfmeier, K. (2014). Forecast evaluation of an observing system simulation experiment assimilating both radar and satellite data. *Monthly Weather Review*, *142*, 107–124. https://doi.org/10.1175/MWR-D-13-00151.1

Jones, T. A., Skinner, P., Yussouf, N., Knopfmeier, K., Reinhart, A., Wang, X., et al. (2020). Assimilation of GOES-16 radiances and retrievals into the Warn-on-Forecast system. *Monthly Weather Review*, *148*, 1829–1859. https://doi.org/10.1175/MWR-D-19-0379.1

Jones, T. A., Wang, X., Skinner, P., Johnson, A., & Wang, Y. (2018). Assimilation of GOES-13 imager clear-sky water vapor (6.5 micron) radiances into a Warn-on-Forecast system. *Monthly Weather Review*, *146*, 1077–1107. https://doi.org/10.1175/MWR-D-17-0280.1

Koenig, M., & de Coning, E. (2009). The MSG global instability indices product and its use as a nowcasting tool. *Weather and Forecasting*, *24*, 272–285. https://doi.org/10.1175/2008WAF2222141.1

Ma, Z., Maddy, E. S., Zhang, B., Zhu, T., & Boukabara, S. A. (2017). Impact assessment of Himawari-8 AHI data assimilation in NCEP GDAS/GFS with GSI. *Journal of Atmospheric and Oceanic Technology.*, *34*, 797–815. https://doi.org/10.1175/JTECH-D-16-0136.1

Minamide, M., & Zhang, F. (2017). Adaptive observation error inflation for assimilating all-sky satellite radiance. *Monthly Weather Review*, *145*, 1063–1081. https://doi.org/10.1175/MWR-D-16-0257.1

Mlawer, E. J., Taubman, S. J., Brown, P. D., Iacono, M. J., & Clough, S. A. (1997). Radiative transfer for inhomogeneous atmospheres: RRTM, a validated correlated-k model for the longwave. *Journal of Geophysical Research*, *102*, 16663–16682. https://doi.org/10.1029/97JD00237

Muller, B. M., & Fuelberg, H. E. (1990). A simulation and diagnostic study of water vapor image dry bands. *Monthly Weather Review*, *118*, 705–722. https://doi.org/10.1175/1520-0493(1990)118<0705:ASADSO>2.0.CO;2

Nakanishi, M., & Niino, H. (2009). Development of an improved turbulence closure model for the atmospheric boundary layer. *Journal of the Meteorological Society of Japan*, *87*, 895–912. https://doi.org/10.2151/jmsj.87.895

NOAA. (2017). Global Ensemble Forecast System (GEFS). [Dataset]. National Oceanographic and Atmospheric Administration. Retrieved from https://www.ncei.noaa.gov/products/weather-climate-models/global-ensemble-forecast

Okamoto, K., McNally, A., & Bell, W. (2014). Progress towards the assimilation of all-sky infrared radiances: An evaluation of cloud effects. *Quarterly Journal of the Royal Meteorological Society*, *140*, 1603–1614. https://doi.org/10.1002/qj.2242

Otkin, J. A., & Potthast, R. (2019). Assimilation of all-sky SEVIRI infrared brightness temperatures in a regional-scale ensemble data assimilation system. *Monthly Weather Review*, *147*, 4481–4509. https://doi.org/10.1175/MWR-D-19-0133.1

Overthaler, A. J., & Markowski, P. M. (2013). A numerical simulation study of the effects of anvil shading on quasi-linear convective systems. *Journal of the Atmospheric Sciences*, *70*, 767–793. https://doi.org/10.1175/JAS-D-12-0123.1

Pan, S., Gao, J., Stensrud, D. J., & Wang, X. (2018). Assimilation of radar radial velocity and reflectivity, satellite cloud water path, and total precipitable water for convective-scale NWP in OSSEs. *Journal of Atmospheric and Oceanic Technology*, *35*, 67–89. https://doi.org/10.1175/JTECH-D-17-0081.1

Roberts, N. M., & Lean, H. W. (2008). Scale-selective verification of rainfall accumulations from high-resolution forecasts of convective events. *Monthly Weather Review*, *136*, 78–97. https://doi.org/10.1175/2007MWR2123.1

Roberts, R. D., & Rutledge, S. (2003). Nowcasting storm initiation and growth using GOES-8 and WSR-88D data. *Weather and Forecasting*, *18*, 562–584. https://doi.org/10.1175/1520-0434(2003)018<0562:nsiagu>2.0.co;2

Schmit, T., Griffith, P., Gunshor, M., Daniels, J., Goodman, S., & Lebair, W. (2017). A closer look at the ABI on the GOES-R series. *Bulletin of the American Meteorological Society*, *98*, 681–698. https://doi.org/10.1175/BAMS-D-15-00230.1

Schröttle, J., Weissmann, M., Scheck, L., & Hutt, A. (2021). Assimilating visible and infrared radiances in idealized simulations of deep convection. *Monthly Weather Review*, *148*, 4357–4375. https://doi.org/10.1175/MWR-D-20-0002.1

Skamarock, W. C., Klemp, J. B., Dudhia, J., Gill, D. O., Barker, D., Duda, M. G., et al. (2008). *A description of the Advanced Research WRF version 3. NCAR Tech. Note NCAR/TN-475+STR*. (p. 113). https://doi.org/10.5065/D68S4MVH

Sobash, R. A., & Wicker, L. J. (2015). On the impact of additive noise in storm-scale EnKF experiments. *Monthly Weather Review*, *143*, 3067–3086. https://doi.org/10.1175/MWR-D-14-00323.1

Stratman, D. R., & Brewster, K. A. (2017). Sensitivities of 1 km forecasts of 24 May 2011 tornadic supercells to microphysics parameterizations. *Monthly Weather Review*, *145*, 2697–2721. https://doi.org/10.1175/MWR-D-16-0282.1

Thompson, G., Field, P. R., Rasmussen, R. M., & Hall, W. D. (2008). Explicit forecasts of winter precipitation using an improved bulk microphysics scheme. Part II: Implementation of a new snow parameterization. *Monthly Weather Review*, *136*, 5095–5115. https://doi.org/10.1175/2008MWR2387.1

Wang, C. P., & Huang, X. (2014). Parallax correction in the analysis of multiple satellite data sets. *Geoscience and Remote Sensing Letters*, *11*, 965–969. https://doi.org/10.1109/LGRS.2013.2283573

Wang, S.-Y., Chen, T.-C., & Taylor, S. E. (2009). Evaluations of NAM forecasts on midtropospheric perturbation-induced convective storms over the U.S. Northern Plains. *Monthly Weather Review*, *24*, 1309–1333. https://doi.org/10.1175/2009WAF2222185.1

Wang, X., & Lei, T. (2014). GSI-based four-dimensional ensemble-variational (4DEnsVar) data assimilation: Formulation and single-resolution experiments with real data for NCEP Global Forecast System. *Monthly Weather Review*, *142*, 3303–3325. https://doi.org/10.1175/MWR-D-13-00303.1

10.1029/2021JD036157

Wang, X., Parrish, D., Kleist, D., & Whitaker, J. (2013). GSI 3DVar-based ensemble-variational hybrid data assimilation for NCEP Global Forecast System: Single-resolution experiments. *Monthly Weather Review*, *141*, 4098–4117. https://doi.org/10.1175/MWR-D-12-00141.1

Wang, Y., & Wang, X. (2017). Direct assimilation of radar reflectivity without tangent linear and adjoint of the nonlinear observation operator in the GSI-based EnVar system: Methodology and experiment with the 8 May 2003 Oklahoma City tornadic supercell. *Monthly Weather Review*, *145*, 1447–1471. https://doi.org/10.1175/MWR-D-16-0231.1

Wang, Y., & Wang, X. (2020). Prediction of tornado-like vortex (TLV) embedded in the 8 May 2003 Oklahoma City tornadic supercell initialized from the subkilometer grid spacing analysis produced by the dual-resolution GSI-based EnVar data assimilation system. *Monthly Weather Review*, *148*, 2909–2934. https://doi.org/10.1175/MWR-D-19-0179.1

Wang, Y., & Wang, X. (2021). Development of convective-scale static background error covariance within GSI-based hybrid EnVar system for direct radar reflectivity data assimilation. *Monthly Weather Review*, *149*, 2713–2736. https://doi.org/10.1175/MWR-D-20-0215.1

Wheatley, D. M., Knopfmeier, K. H., Jones, T. A., & Creager, G. J. (2015). Storm-scale data assimilation and ensemble forecasting with the NSSL experimental Warn-on-Forecast System. Part I: Radar data experiments. *Weather and Forecasting*, *30*, 1795–1817. https://doi.org/10.1175/WAF-D-15-0043.1

Whitaker, J. S., & Hamill, T. M. (2002). Ensemble data assimilation without perturbed observations. *Monthly Weather Review*, *130*, 1913–1924. https://doi.org/10.1175/1520-0493(2002)130<1913:edawpo>2.0.co;2(2002)130<1913:EDAWPO>2.0.CO;2

Whitaker, J. S., & Hamill, T. M. (2012). Evaluating methods to account for system errors in ensemble data assimilation. *Monthly Weather Review*, *140*, 3078–3089. https://doi.org/10.1175/MWR-D-11-00276.1

Whitaker, J. S., Hamill, T. M., Wei, X., Song, Y., & Toth, Z. (2008). Ensemble data assimilation with the NCEP global forecast system. *Monthly Weather Review*, *136*, 463–448. https://doi.org/10.1175/2007MWR2018.1

WRF-ARW. (2017). Weather Research and Forecasting model, Advanced Research WRF. Version 3.9.1. [Software]. WRF-ARW. https://doi.org/10.5065/D6MK6B4K

Xu, D., Liu, Z., Fan, S., Chen, M., & Shen, F. (2021). Assimilating all-sky infrared radiances from Himawari-8 using the 3DVar method for the prediction of a severe storm over north China. *Advances in Atmospheric Sciences*, *38*, 661–676. https://doi.org/10.1007/s00376-020-0219-z

Yussouf, N., Mansell, E. R., Wicker, L. J., Wheatley, D. M., & Stensrud, D. J. (2013). The ensemble Kalman filter analyses and forecasts of the 8 May 2003 Oklahoma City tornadic supercell storm using single- and double-moment microphysics schemes. *Monthly Weather Review*, *141*, 3388–3412. https://doi.org/10.1175/MWR-D-12-00237.1

Zhang, J., Howard, K., Langston, C., Kaney, B., Qi, Y., Tang, L., et al. (2016). Multi-Radar Multi-Sensor (MRMS) quantitative precipitation estimation: Initial operating capabilities. *Bulletin of the American Meteorological Society*, *97*, 621–638. https://doi.org/10.1175/BAMS-D-14-00174.1

Zhang, Y., Stensrud, D. J., & Zhang, F. (2019). Simultaneous assimilation of radar and all-sky satellite infrared radiance observations for convection-allowing ensemble analysis and prediction of severe thunderstorms. *Monthly Weather Review*, *147*, 4389–4409. https://doi.org/10.1175/MWR-D-19-0163.1

Zhang, Y., Zhang, F., & Stensrud, D. J. (2018). Assimilating all-sky infrared radiances from GOES-16 ABI using an ensemble Kalman filter for convection-allowing severe thunderstorms predictions. *Monthly Weather Review*, *146*, 3363–3381. https://doi.org/10.1175/MWR-D-18-0062.1

Zhou, X., Zhu, Y., Hou, D., Luo, Y., Peng, J., & Wobus, R. (2017). Performance of the new NCEP global ensemble forecast system in a parallel experiment. *Weather and Forecasting*, *32*, 1989–2004. https://doi.org/10.1175/WAF-D-17-0023.1

Zhu, Y., Liu, E., Mahajan, R., Thomas, C., Groff, D., Van Delst, P., et al. (2016). All-sky microwave radiance assimilation in NCEPs GSI analysis system. *Monthly Weather Review*, *144*, 4709–4735. https://doi.org/10.1175/MWR-D-15-0445.1

Zhu, Y., Gayno, G., Purser, R. J., Su, X., & Yang, R. (2019). Expansion of the all-sky radiance assimilation to ATMS at NCEP. *Monthly Weather Review*, *147*, 2603–2620. https://doi.org/10.1175/MWR-D-18-0228.1